

Beyond MMSE: Enhancing PnP Restoration with ProxiMAP

Kenta Vert^{1,*} Giacomo Meanti^{1,2,*}
Scott Pesme¹ Michael Arbel¹ Julien Mairal¹

{firstname.lastname}@inria.fr

*Equal contribution

¹Univ. Grenoble Alpes, Inria, CNRS, Grenoble INP, LJK

²MaLGa Centre, DIBRIS, Università di Genova, MMS, Italian Institute of Technology, Genova, Italy

Abstract

Plug-and-Play (PnP) methods have become standard tools for solving imaging inverse problems by replacing the intractable maximum a posteriori (MAP) denoiser with the MMSE one. While this mismatch has been widely treated as unavoidable, recent works have sought to close this gap by targeting the MAP with diffusion-model scores. We show this is problematic in practice: learned scores do not match the true ones, so MAP-targeting iterations converge to cartoon-like images rather than realistic ones, and better results are obtained by stopping short of convergence. We turn this observation into a design principle and introduce **ProxiMAP**, an iterative MAP approximation whose noise schedule keeps the iterate’s residual noise matched to the denoiser’s training noise. This keeps the denoiser in-distribution where its score is reliable, and yields implicit early stopping that avoids the failure mode above. **ProxiMAP** is a modular drop-in replacement for MMSE denoisers in standard PnP algorithms and consistently sharpens reconstructions across deblurring, inpainting, super-resolution, and phase retrieval. Building on the same principle, we propose a hybrid variant that applies **ProxiMAP** only in the late iterations of PnP, where the denoiser is most reliable—matching or exceeding the full-replacement variant at a fraction of the cost.

1 Introduction

Inverse problems are ubiquitous in imaging, sharing the mathematical structure $y = \mathcal{A}(x) + \epsilon$, where x is the unknown clean image, \mathcal{A} a known degradation operator (*e.g.*, blur, subsampling), and ϵ measurement noise. This common structure has motivated general-purpose frameworks such as Plug-and-Play (PnP) (Venkatakrisnan et al., 2013; Chan et al., 2016) and Regularization by Denoising (RED) (Romano et al., 2017), which combine optimization with powerful image priors.

Adopting a probabilistic perspective, recovery of x from y is formulated as posterior maximization:

$$x^* = \arg \max_x p(x | y) = \arg \max_x \log p(y | x) + \log p(x), \quad (1)$$

or, equivalently, as $x^* = \arg \min_x f(x, y) + \lambda g(x)$, with f a data-fidelity term, g a regularizer reflecting prior knowledge, and $\lambda > 0$ balancing the two. Such composite problems, when f is strongly convex but g is not, can be solved with proximal splitting methods such as ADMM and HQS (Combettes and Pesquet, 2011; Parikh and Boyd, 2014) which rely on the proximal operator

$$\text{prox}_{\tau g}(z) := \arg \min_x \frac{1}{2} \|x - z\|^2 + \tau g(x). \quad (2)$$

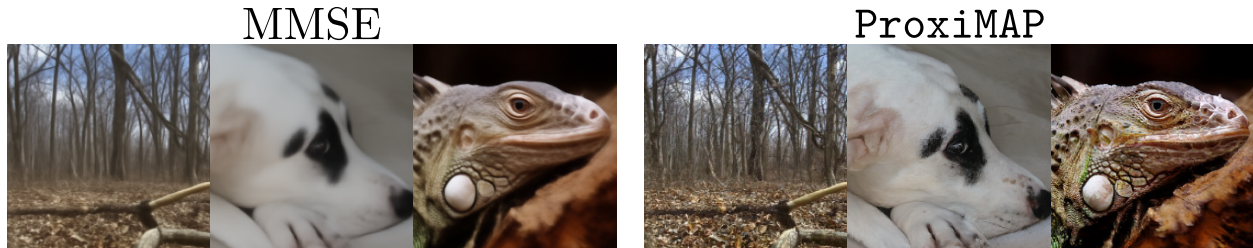


Figure 1: Conditional MMSE estimates (left) versus ProxiMAP (right) on three crops at noise level $\sigma_y = 0.2$. ProxiMAP recovers fine textures and sharp edges that the MMSE estimator smooths away. We propose to leverage this improvement for PnP image reconstruction.

The key insight underlying PnP is that when $g = -\log p$, the proximal operator (2) is the maximum a posteriori (MAP) denoiser of a Gaussian denoising problem. This motivates replacing g with a denoiser D_θ which can be a deep neural network trained on large natural image datasets (Zhang et al., 2017) in order to capture an expressive prior. In practice, however, D_θ is trained with a squared-error loss $\mathbb{E}_{x,\epsilon} \|D_\theta(x+\sigma\epsilon) - x\|^2$, and the trained model will approximate the MMSE estimator $\mathbb{E}[X | Y = x + \sigma\epsilon]$ rather than the MAP that (1) actually requires. The practical consequence is the well-known *regression-to-the-mean* oversmoothing of MMSE-based reconstructions.

Why MAP-targeting fails, and what to do instead. A natural way to close this gap is to estimate the MAP denoiser directly. Laumont et al. (2023) and Pesme et al. (2025) have shown convergence properties of a smoothed version of gradient descent on the proximal objective, using scores $\nabla_x \log p_\sigma(x)$ and annealing $\sigma \rightarrow 0$. With *exact* scores and log-concave p , this procedure recovers the true MAP. In Section 3.1, we use a Gaussian mixture model, where the score is available in closed form, to verify that the recovery is clean. However, when the scores are learned from data, the procedure converges to a different object: the MAP of the learned distribution, whose high-density regions, due to the implicit biases of diffusion training, do not coincide with those of the true data distribution. The resulting images are cartoon-like (also reported by Karczewski et al. (2025)), and better reconstructions are obtained by stopping short of convergence. We turn this observation into a design principle for MAP approximation under inexact scores: at every step, the iterate’s residual noise level should match the noise level at which the denoiser is queried. A learned denoiser is reliable only on inputs whose noise statistics match its training distribution; outside that regime its score estimate degrades, which leads to the failure mode above. We introduce ProxiMAP, an iterative MAP approximation that follows this principle. The matching constraint determines the noise schedule, keeps the denoiser in-distribution throughout, and yields implicit early stopping preventing drift into the failure regime. The result is sharper than the MMSE estimator, as illustrated in Fig. 1.

ProxiMAP is a modular drop-in replacement for MMSE denoisers in standard PnP algorithms. We integrate it into three state-of-the-art PnP algorithms (DPIR, DiffPIR, DAPS) and show consistent LPIPS improvements with competitive PSNR across deblurring, inpainting, super-resolution, phase retrieval, and HDR reconstruction, on both FFHQ and ImageNet. Pushing the matching principle further, we propose a hybrid variant that uses MMSE denoisers early in PnP and switches to ProxiMAP only at the end – motivated by the observation that PnP iterates enter the regime of reliable score information only in their later iterations. The hybrid recovers most of the gains of the full-replacement variant at a fraction of the cost – and in several cases improves on it.

In summary, our main contributions are:

- **A diagnosis of MAP estimation under learned priors.** Via a controlled comparison between

a diffusion model and a Gaussian mixture model where exact scores are available, we show that the cartoon-like artifacts produced by naïve MAP iteration stem from score approximation error rather than from MAP estimation itself. As a consequence, better reconstructions are obtained by stopping short of convergence.

- **An effective algorithm derived from a single principle.** ProxiMAP is an iterative MAP approximation whose noise and step-size schedules follow from matching the iterate’s residual noise to the denoiser’s training noise at every step. This keeps the denoiser in-distribution and yields implicit early stopping, providing better approximation under inexact scores.
- **Systematic improvements over PnP baselines** across multiple algorithms, tasks, datasets, and noise levels, established via Bayesian hyperparameter optimization to ensure fair comparison.
- **An efficient and practical hybrid variant** that uses ProxiMAP only in the late iterations of PnP, matching or exceeding full-replacement ProxiMAP at substantially reduced cost.

2 Related Work

Plug-and-play (PnP) methods. PnP methods (Venkatakrishnan et al., 2013) replace the proximal operator in iterative optimisation algorithms with a generic denoiser $D_\theta(y)$, typically parameterised by the noise level σ . This decoupling of the data-fidelity term from the prior allows to leverage off-the-shelf denoisers as implicit image priors. A wide variety of denoisers have been used within this framework, including classical approaches such as BM3D (Dabov et al., 2007), convolutional neural networks (Meinhardt et al., 2017; Zhang et al., 2021, 2017), and, more recently, diffusion models (Graikos et al., 2022; Zhu et al., 2023) as well as flow matching models (Martin et al., 2025). Different proximal optimisation schemes can be used, such as PGD (Terris et al., 2020), ADMM (Romano et al., 2017), and HQS (Zhang et al., 2017). As the PnP literature is vast, we refer the reader to Hurault (2023); Kamilov et al. (2023) for a comprehensive overview. Convergence of PnP algorithms has been established under various assumptions on the denoiser (Sreehari et al., 2016; Gavaskar and Chaudhury, 2020; Nair et al., 2021; Xu et al., 2020; Hurault et al., 2022). However, standard deep denoisers approximate the MMSE estimator rather than the proximal operator of the true prior, so the recovered solution cannot in general be interpreted as a MAP estimate.

MAP estimation with learned priors. Several recent works have recognized the limitations of MMSE-based denoisers and proposed to estimate the proximal operator $\text{prox}_{-\tau \ln p}$ or, equivalently, the MAP denoiser, directly. Fang et al. (2024) replace the standard MSE objective with a regularized proximal matching loss whose minimizer coincides, as the regularization parameter tends to zero, with the proximal operator. Laumont et al. (2023) introduce PnP-SGD, which performs stochastic gradient descent on a smoothed version of the proximal objective; by keeping the smoothing parameter fixed, their method approximates the proximal operator of the smoothed density rather than the true one. To overcome this limitation, Pesme et al. (2025) leverage diffusion-model score estimates $\nabla \ln p_{\sigma_k}$ across multiple noise levels and analyze a smoothed gradient descent algorithm with annealed σ_k , proving convergence to the true proximal operator under a log-concavity assumption.

A parallel line of work formulates inverse problems as MAP estimation directly within the diffusion-sampling framework. Gutha et al. (2025a) cast the reverse conditional generation as optimization of a tractable MAP objective, and develop algorithms for inpainting; Gutha et al. (2025b) build on this with a variational mode-seeking loss whose per-step minimization guides samples toward the MAP estimate. Zhang et al. (2025b) propose Local MAP Sampling, a covariance approximation that unifies Tweedie-moment-projected diffusion (Boys et al., 2025) with optimization-based methods. These works produce end-to-end inverse problem solvers and do not address the problem we consider: enhancing existing PnP frameworks via a modular replacement of their inner

denoising step.

Sampling-based methods. An alternative to optimization-based PnP methods is to sample from the posterior $p(x | y)$ rather than seek its maximum. A prominent class are *conditional diffusion models*, which modify the unconditional score $\nabla \ln p_\sigma(x)$ into the posterior score $\nabla \ln p_\sigma(x | y)$, then sample via the reverse diffusion SDE. Various approximations make this tractable: Dhariwal and Nichol (2021) use a pretrained classifier to estimate $\nabla \ln p(y | x)$; Jalal et al. (2021) approximate $p_\sigma(y | x) \approx p(y | x)$ via a Gaussian likelihood; DPS (Chung et al., 2023) approximates the posterior mean using Tweedie’s formula; and Boys et al. (2025) further approximate the posterior standard deviation. Similarly, Kadkhodaie and Simoncelli (2020) draw high-density samples by annealing the noise level and taking gradient steps. All these methods target the posterior distribution rather than its mode. Relatedly, the InDI algorithm of Delbracio and Milanfar (2023) is an iterative restoration method linked to the probability-flow ODE via Tweedie’s formula.

3 The ProxiMAP Algorithm

We begin by showing that with learned diffusion models the MAP solution for the denoising problem drifts towards unrealistic regions in image-space. In Section 3.2 we derive **ProxiMAP** as a way of avoiding such drift and in Section 3.3, we discuss **ProxiMAP** in the context of PnP frameworks.

3.1 MAP-targeting fails with learned scores

Once again, we wish to compute the proximal operator of a noisy image $y = x + \sigma_y \epsilon$, $\epsilon \sim \mathcal{N}(0, I)$

$$\text{prox}_{-\tau \log p}(y) := \arg \min_x \frac{1}{2} \|x - y\|^2 - \tau \log p(x), \tag{3}$$

where $p(x)$ is the unknown density of natural images and τ controls regularization strength. With access to the score $\nabla \log p(x)$ one could solve (3) by gradient descent. In practice we only have approximate scores $\nabla \log p_\sigma(x)$ of the smoothed densities $p_\sigma = p * \mathcal{N}(0, \sigma^2 I)$, obtained from a pretrained diffusion model. As $\sigma \rightarrow 0$, the smoothed scores approach the true $\nabla \log p$, but the objective becomes increasingly non-smooth and gradient descent at fixed small σ is unstable. Pesme et al. (2025) proposed to solve Eq. (3) using smoothed gradient descent with decreasing σ_k :

$$x_{k+1} = x_k - \gamma_k \nabla_x \left(\frac{1}{2} \|x_k - y\|^2 - \tau \log p_{\sigma_k}(x_k) \right), \tag{4}$$

and proved convergence to the MAP under log-concavity of p and with the following schedule:

$$\sigma_k^2 = \frac{\tau}{k+1}, \quad \gamma_k = \frac{1}{k+2} \implies x_{k+1} = \frac{y}{k+2} + \frac{k+1}{k+2} \mathbb{E}[X | X_{\sigma_k} = x_k]. \tag{5}$$

Although the assumption does not hold for natural images, Eq. (5) is a direct and theoretically grounded MAP-targeting iteration, and we use it as the diagnostic vehicle here. We show below that replacing the exact MMSE (not available in practice) by a score-based approximation yields a failure mode at convergence.

The cartoon effect. We instantiate (5) with three pretrained denoisers: a flow-matching model on MNIST and unconditional diffusion models on FFHQ and ImageNet. Across all three (Fig. 2), the resulting iterates do not resemble typical image samples. On MNIST the MAP estimates progressively thicken into blob-like shapes as σ_y increases, in contrast to the overly smooth MMSE estimates. On FFHQ and ImageNet, iterates exhibit the *cartoon* appearance recently reported

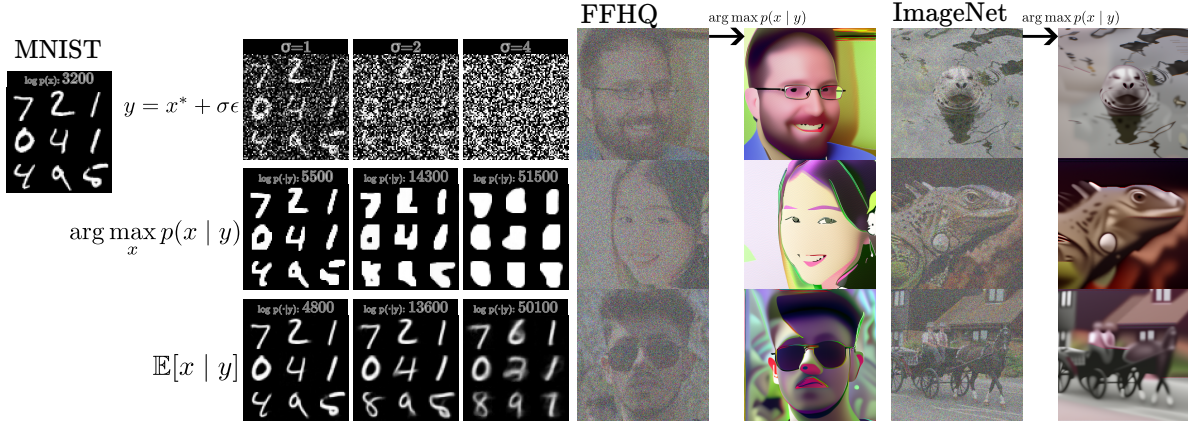


Figure 2: The MAP approximation procedure of Eq. (5) with *learned scores* yields cartoon-like outputs on natural-image datasets (right) and blob-like digits on MNIST (left). For MNIST we show the noisy data (top), along with MAP estimates (middle) and MMSE estimates (bottom). Conditional log-probability of the MAP estimates is always higher than that of the MMSE.

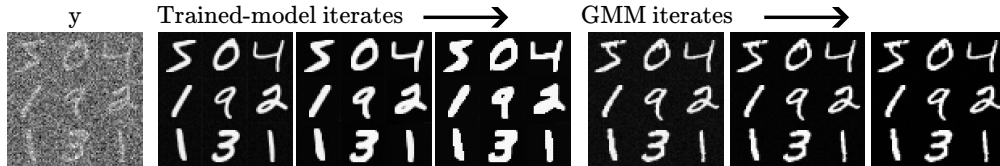


Figure 3: Iterates of Eq. (5) with the score from a diffusion model (left) or from a GMM (right). With exact scores the iteration recovers clean modes; with learned scores it drifts to cartoon outputs.

by Karczewski et al. (2025) for pretrained diffusion models: flat colors, exaggerated edges, and unrealistic textures.

The crucial observation is that this is genuinely posterior maximization, not algorithmic failure. To verify this, we computed the conditional log-likelihood of each image under the learned MNIST model using the augmented Probability-Flow ODE (Song et al., 2021b; Chen et al., 2018). The values, superimposed on Fig. 2 (left), confirm that iterates of Eq. (5) have higher probability than the MMSE estimates, despite looking unrealistic. The cartoon images are what the model considers most likely given the noisy input. Now, either (a) high-density regions of the learned distribution genuinely contain non-typical images because of the implicit biases of diffusion model training (Kamb and Ganguli, 2025), or (b) gradient descent on the non-convex landscape gets stuck in poor local maxima. To distinguish these, we replace the trained model with a Gaussian mixture model (GMM) centered on the training set with small isotropic variance and for which $\nabla \log p_{\sigma_k}$ is available in closed form. The GMM has a non-convex probability distribution so any algorithmic pathology of GD due to non-convexity should manifest here as well. Running (5) with the exact GMM score, however, yields realistic images (the modes of the GMM) independently of initialization, while the same algorithm with the diffusion-model score produces cartoon outputs (Fig. 3). Non-convexity is therefore not the issue. The cartoon effect is a property of the *learned* score, whose zeros are displaced from those of the true distribution by the implicit biases of diffusion model training. As a further check, in Section B we train a diffusion model in the *memorizing regime* (Biroli et al., 2024)—where the model has effectively recovered the empirical score—and find that MAP estimates from (5) are then artifact-free. Section A discusses broader implications for MAP estimation under learned priors.

Implication for algorithm design. The diagnosis suggests two things. First, the failure is not intrinsic to MAP estimation: with exact scores the procedure works. Second, the failure occurs as the iteration converges: early iterates of (5) typically resemble plausible images. In the next section we address how to stop short of convergence in a principled way.

3.2 The ProxiMAP algorithm

We wish to develop an algorithm which targets the MAP objective while keeping iterates in a regime where the denoiser is reliable: the residual noise in x_k should match the noise level σ_k at which the denoiser is queried. ProxiMAP achieves this by exploiting a structural property of the smoothed GD recursion (4), initialized at $x_0 = y$.

Tracking residual noise. Treating each denoiser output as noiseless and writing σ_y for the standard deviation of y , the recursion can be analyzed term by term:

$$\underbrace{x_{k+1}}_{\sigma_{k+1}} = \left(1 - \gamma_k \left(1 + \frac{\tau}{\sigma_k^2}\right)\right) \underbrace{x_k}_{\sigma_k} + \gamma_k \underbrace{y}_{\sigma_y} + \frac{\tau \gamma_k}{\sigma_k^2} \underbrace{\mathbb{E}[X \mid X_{\sigma_k} = x_k]}_0.$$

Since $x_0 = y$ and successive denoiser outputs carry no noise, the noisy component of every x_k remains a multiple of y . Standard deviations therefore combine linearly, giving

$$\sigma_{k+1} = \left(1 - \gamma_k \left(1 + \frac{\tau}{\sigma_k^2}\right)\right) \sigma_k + \gamma_k \sigma_y. \quad (6)$$

This expression gives the residual noise level of x_k as a function of the schedule. Using σ_k from (6) as the noise conditioning at step k ensures that the denoiser always operates on in-distribution inputs.

Step-size choice. The smoothed objective $x \mapsto \frac{1}{2}\|x - y\|^2 - \tau \log p_{\sigma_k}(x)$ at step k is L_{σ_k} -smooth with $L_{\sigma_k} = 1 + \tau/\sigma_k^2$ (Pesme et al., 2025). The standard step-size for L -smooth objectives is $\gamma_k = \beta/L_{\sigma_k}$ with $\beta \in (0, 1)$ a hyperparameter, which yields

$$\sigma_{k+1} = (1 - \beta)\sigma_k + \frac{\beta}{1 + \tau/\sigma_k^2}\sigma_y, \quad \gamma_k = \frac{\beta}{L_{\sigma_k}}. \quad (7)$$

For the algorithm to recover a sharp image we need $\sigma_k \rightarrow 0$, which (Lemma 1 in Section C) requires $\tau > \sigma_y^2/4$. We parametrize $\tau = \tau_{\text{mul}} \cdot \sigma_y^2/4$ with $\tau_{\text{mul}} > 1$ to guarantee this. A noise-matching motivation also appears in the SNORE algorithm (Renaud et al., 2024), where it is used for stochastic regularization rather than as the constraint for a deterministic MAP-targeting schedule.

Pseudocode and hyperparameters. The pseudocode for ProxiMAP is given in Algorithm 1, with main hyperparameters τ_{mul} , β , and K . To minimize tuning efforts, we fix $\tau_{\text{mul}} = 10$ as it only influences the learning rate which we tune through σ_K . We fix the number of iterations to $K = 8$, following a denoising experiment which revealed that perceptual quality (LPIPS) saturates beyond this point (see Section 4.1). We choose β so that the final variance σ_K^2 attains a prescribed value given σ_y , K , and τ_{mul} . The final variance is therefore the only hyperparameter actively tuned in practice; a typical tuning range is $\sigma_K \in [0.001, 0.1]$. Finally, we return the last MMSE estimate $\hat{x}_K^{\text{MMSE}} = D_\theta(x_{K-1}, \sigma_{K-1})$ since it provides a final noise-free output, whereas x_K still contains a residual scaled version of y .

ProxiMAP as principled early stopping. Denote by $\hat{\sigma}(x_k)$ the residual noise present in any iterate x_k , computed like before by treating denoiser outputs as noiseless. The iteration of Eq. (5) uses a mismatched noise schedule $\sigma_k > \hat{\sigma}(x_k)$ for $k > 1$, in order to show convergence to the MAP. The ProxiMAP schedule of Eq. (7) instead enforces $\sigma_k = \hat{\sigma}(x_k)$ for all k . Since the step-size γ_k shrinks

Algorithm 1 The ProxiMAP algorithm. Input: noisy image y (noise variance σ_y^2) and a trained denoiser D_θ . Output: approximate MAP denoising solution.

Require: $\tau_{\text{mul}}, \sigma_y, y, \beta, K$, denoiser D_θ

- 1: $(x_0, \sigma_0) \leftarrow (y, \sigma_y)$
 - 2: $\tau \leftarrow \tau_{\text{mul}} \frac{\sigma_y^2}{4}$ and $\gamma_0 \leftarrow \frac{\beta}{1+\tau/\sigma_0^2}$
 - 3: **for** $k = 0, \dots, K - 1$ **do**
 - 4: $\hat{x}_{k+1}^{\text{MMSE}} \leftarrow D_\theta(x_k, \sigma_k)$
 - 5: $x_{k+1} \leftarrow (1 - \gamma_k(1 + \tau/\sigma_k^2))x_k + \gamma_k x_0 + \frac{\tau\gamma_k}{\sigma_k^2} \hat{x}_{k+1}^{\text{MMSE}}$
 - 6: $\sigma_{k+1} \leftarrow (1 - \gamma_k(1 + \tau/\sigma_k^2))\sigma_k + \gamma_k \sigma_y$
 - 7: $\gamma_{k+1} \leftarrow \frac{\beta}{1+\tau/\sigma_{k+1}^2}$
 - 8: **end for**
 - 9: **return** \hat{x}_K^{MMSE} ▷ final denoiser call applied to x_{K-1} at noise level σ_{K-1}
-

together with σ_k , the iteration slows down as it approaches the data manifold, avoiding mismatched queries which lead to artifacts, and ensuring stable results in few steps. ProxiMAP is therefore not a more accurate approximation of the learned MAP; it is an explicit mechanism for stopping short of it.

3.3 ProxiMAP in PnP algorithms

Having established that ProxiMAP performs effectively as a MAP denoiser, we next integrate it into PnP inverse problem solvers by replacing the standard MMSE estimator in their inner loop. Among many existing PnP algorithms (Kamilov et al., 2023; Li et al., 2025), we select three representatives:

- DPIP (Zhang et al., 2021) is based on half-quadratic splitting with a schedule that yields good results in few iterations.
- DiffPIP (Zhu et al., 2023) improves the performance of DPIP on generative tasks such as block inpainting by introducing a *noise-addition* step on top of existing data-fidelity and denoising steps. The added noise goes to 0 during optimization.
- DAPS (Zhang et al., 2025a) replaces the denoising step with an iterative procedure which samples from $p(x | x_{\sigma_t})$. Since the inner loop of DAPS already requires multiple evaluations of the model, ProxiMAP does not introduce any computational overhead.

For the first two, we keep the same iteration and scheduling and replace calls to the denoiser D_θ with calls to ProxiMAP. For DAPS we replace the call to the diffusion sampling algorithm, and modify the outer noise schedule to match Eq. (6). Algorithm details are provided in Section D.

Fast hybrid variant. Because ProxiMAP’s computational cost scales with the number of inner iterations K , replacing every MMSE call in a PnP outer loop with a full ProxiMAP call is expensive. The noise-matching analysis above suggests a natural way to reduce this cost while preserving its benefits: apply ProxiMAP only in the late iterations of the PnP outer loop, where the iterate’s residual noise is low and the denoiser’s score estimate is most reliable. In the early iterations, the iterate is still far from the data manifold, the score estimate is less critical, and a single MMSE call suffices. We refer to this as the *hybrid variant* of ProxiMAP+PnP. When applying ProxiMAP do the last PnP iteration, we call the corresponding variant **Fast ProxiMAP**. Section 4 shows that the hybrid variant matches or exceeds the full-replacement variant at substantially reduced cost.

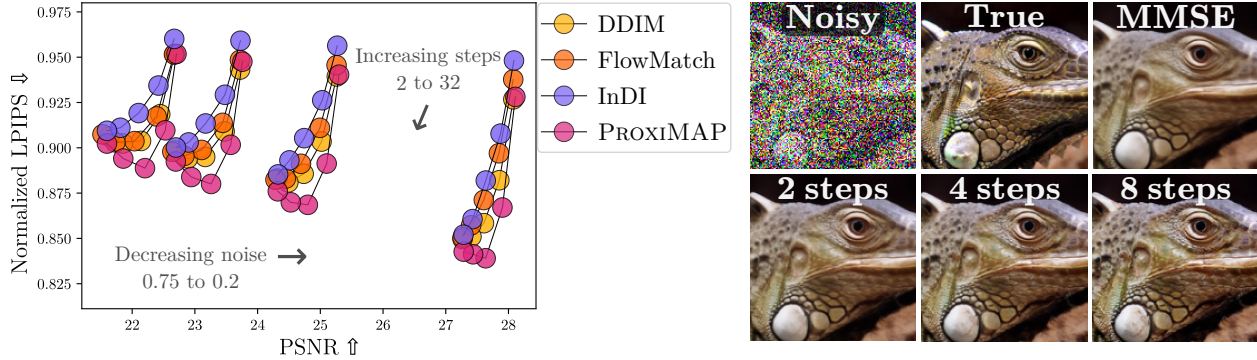


Figure 4: (left) PSNR and LPIPS (normalized so the MMSE estimator’s LPIPS is 1) across noise levels and step counts for `ProxiMAP` and three conditional samplers on ImageNet. `ProxiMAP` dominates the others by remaining closest to the (high-PSNR, low-LPIPS) corner. (right) Outputs of `ProxiMAP` for increasing K (the MMSE estimator is the $K = 1$ case). Results on FFHQ are in Fig. 8.

4 Experiments

4.1 Validating the algorithm: standalone denoising

We begin by characterizing `ProxiMAP` as a standalone denoiser, both to compare it to other diffusion-based denoising algorithms, and to determine the iteration count K to be used in the subsequent PnP experiments. Given $y = x + \sigma_y \epsilon$ with $\epsilon \sim \mathcal{N}(0, I)$, the goal is to recover x . The denoiser D_θ is a diffusion model from Dhariwal and Nichol (2021) trained on ILSVRC-2012 (ImageNet). We compare `ProxiMAP` to the conditional MMSE estimate $D_\theta(y, \sigma_y) \approx \mathbb{E}[X | X_{\sigma_y} = y]$ and to three deterministic diffusion samplers adapted to the conditional setting: DDIM (Song et al., 2021a), Flow Matching (Liu et al., 2023; Albergo and Vanden-Eijnden, 2023), and InDI (Delbracio and Milanfar, 2023). Each sampler is initialized from the timestep corresponding to y according to the original sampler’s schedule, rather than from the initial timestep which corresponds to pure noise. Performance is evaluated in terms of distortion (PSNR, corresponding to pixel-wise accuracy, higher is better) and perception (LPIPS, correlating with the human perception of sharpness, lower is better); Additional details are provided in Section E.

Figure 4 shows two consistent patterns. First, all iterative methods improve LPIPS over the MMSE estimator while degrading PSNR. This is the standard perception-distortion trade-off (Blau and Michaeli, 2018). Second, `ProxiMAP` dominates the conditional samplers across all step counts and noise levels, sitting strictly closer to the optimal corner of the plane. LPIPS improvement saturates beyond 8 steps for `ProxiMAP` while computational cost grows linearly, which is confirmed by Figure 8 from Section H on the FFHQ dataset; we therefore use $K = 8$ throughout the rest of the paper.

4.2 PnP experiments

We next evaluate `ProxiMAP` as a drop-in replacement for the MMSE denoiser in the three state-of-the-art PnP frameworks we introduced in Section 3.3: `DPIR`, `DiffPIR`, and `DAPS`. All experiments use FFHQ (Karras et al., 2019) and ImageNet (Deng et al., 2009) samples at 256×256 resolution; the underlying diffusion models are fixed (the network of Choi et al. (2021) for FFHQ and the unconditional model of Dhariwal and Nichol (2021) for ImageNet). For `DPIR` and `DiffPIR`, we keep the outer loop unchanged (20 iterations) and replace each MMSE call with $K = 8$ inner `ProxiMAP` iterations except for the `Fast` variant that only calls `ProxiMAP` for the last PnP iteration resulting

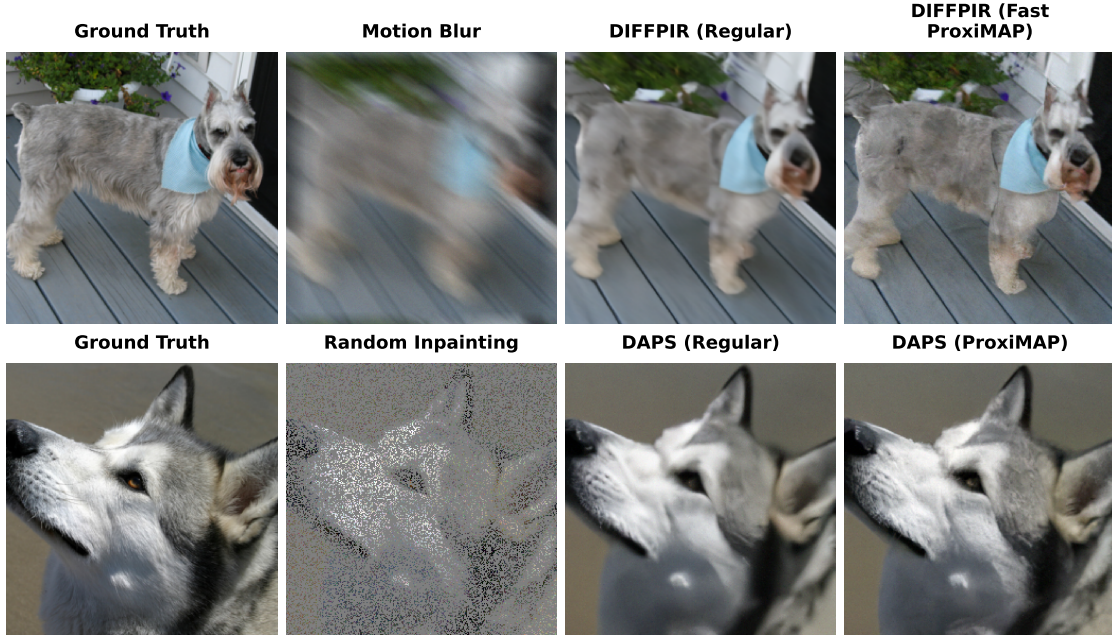


Figure 5: Examples of image restoration from ImageNet illustrating the detail enhancing effect of ProxiMAP already see in the denoising task of Figure 4. Other examples can be found in Section H.

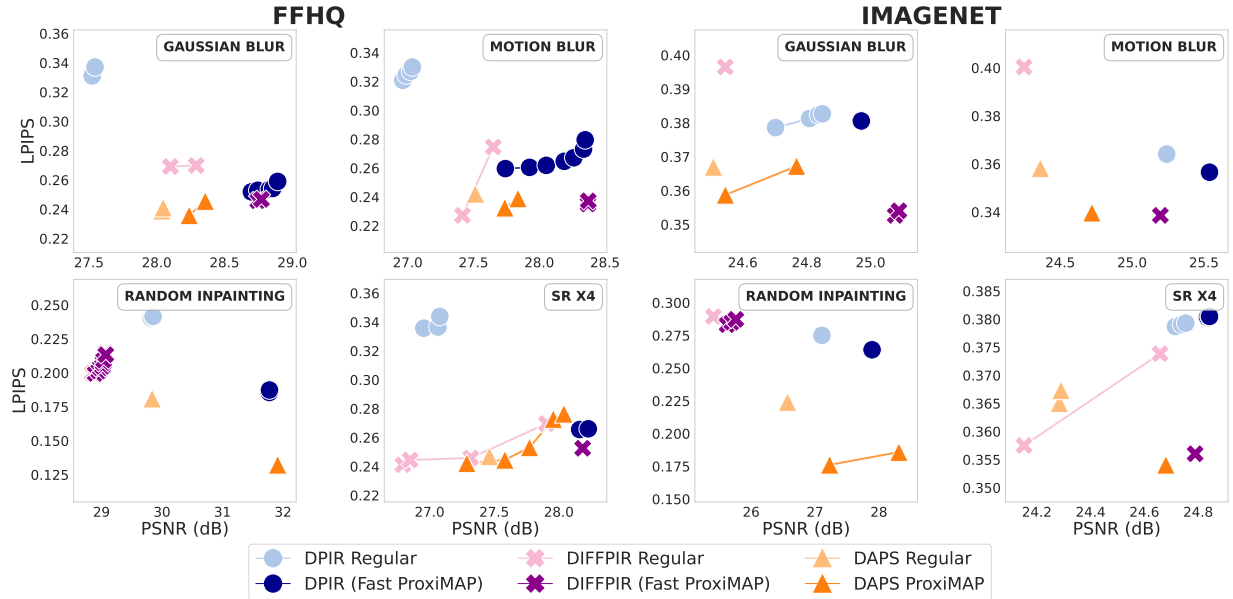


Figure 6: Three PnP algorithms versus their ProxiMAP counterparts on four inverse problems. Lighter colors are baselines; darker colors are ProxiMAP variants. ProxiMAP shifts the Pareto fronts toward the optimal (high-PSNR, low-LPIPS) corner across nearly all settings.

to only 7 additional calls to the denoiser. DAPS’s inner loop already runs an iterative sampling procedure, which we replace by 6 ProxiMAP iterations at no additional cost. We consider several tasks for the evaluation, which are detailed in Section F.

Automatic hyperparameter tuning protocol. PnP methods are sensitive to hyperparameter choices, which are usually changed depending on the task and the noise level. However, reporting is often inconsistent in the literature. For example, certain papers (Zhu et al., 2023; Mardani et al., 2024) scale images to $[0, 1]$ while others (Martin et al., 2025; Alkhouri et al., 2025) use $[-1, 1]$, leading to noise levels that do not match. To allocate the same tuning budget to every method, we run Bayesian optimization (BO) for each $(dataset, algorithm, problem)$ triplet using the Ax library (Olson et al., 2025) with 15 random-search iterations followed by 15 BO iterations, optimizing both LPIPS and PSNR on a held-out tuning set of 30 images. Using the hyperparameters lying on the Pareto front which results from BO, we then compute all metrics on a separate test-set of 70 images. Full hyperparameter ranges and tuning details for every method are provided in Section G.

The hybrid variant: better and cheaper. Because ProxiMAP serves as a strictly more accurate denoiser than MMSE, it naturally acts as a drop-in replacement in standard PnP algorithms. However, because of the double loop, a full replacement of MMSE with ProxiMAP increases the number of function evaluations (NFEs) of DPIP and DiffPIP by a factor of 8. The noise-matching analysis (Section 3.2) suggests this is unnecessary: only the late iterations of a PnP outer loop operate in the regime where ProxiMAP’s reliance on score accuracy pays off. We therefore introduce the hybrid variant, which we call Fast ProxiMAP: it uses MMSE denoising for the first n outer iterations of DPIP and DiffPIP and switches to ProxiMAP for the remaining $20 - n$. Empirically, $n = 19$ works best across tasks. The corresponding study is presented in Fig. 10 and Fig. 11 of Section H.

Drop-in replacement. The full-replacement and Fast ProxiMAP variants are compared in Table 1 alongside four further diffusion-based PnP algorithms (DPS (Chung et al., 2023), SITCOM (Alkhouri et al., 2025), REDDiff (Mardani et al., 2024), and PnPFlow (Martin et al., 2025)). Furthermore, Fig. 6 shows the perception-distortion plane for six inverse problems with noise level $\sigma_y = 0.05$ (see also Fig. 9 from Section H). Fast ProxiMAP matches or exceeds the full-replacement variant on most settings, with particularly strong gains for DiffPIP, while reducing NFEs from 160 to 27, a reasonably small overhead over the baseline approach (NFE=20). We do not apply Fast ProxiMAP to DAPS, whose inner loop is structurally different (sampling) and whose ProxiMAP-augmented variant already runs only 6 inner iterations. Further details, additional visual results, and discussion on failure cases are provided in Section H. Across this comparison, the ProxiMAP-augmented methods are competitive with the state of the art and frequently best on the perception-distortion frontier. No single method dominates every task, which reflects both the perception-distortion trade-off (Blau and Michaeli, 2018) and the genuine heterogeneity of the problems. This is precisely why the across-the-board improvements provided by ProxiMAP, and especially Fast ProxiMAP, matter: rather than a new specialized algorithm, our contribution is a modular component that lifts the perception axis of an entire family of existing methods.

5 Conclusion

PnP methods replace the MAP denoiser their variational formulation prescribes with an MMSE denoiser, producing the well-known oversmoothing of posterior-mean estimators. We showed that simply targeting the MAP with diffusion-model scores does not resolve this: with learned scores, MAP-targeting iterations drift toward unrealistic regions of the learned distribution, and a controlled comparison with exact GMM scores confirms that this is a property of the learned score, not of MAP estimation itself. Our ProxiMAP algorithm addresses this issue: Used as a drop-in replacement for

Table 1: Summary of results on the ImageNet dataset. We pick the HP sample from the Pareto front with the lowest LPIPS. Empty cells: DPIR and DiffPIR require a closed-form proximal step and so do not apply to non-linear tasks. NFEs are doubled for methods requiring backward passes. Colors indicate whether the ProxiMAP variant is **better than**, **tied with**, or **worse than** the corresponding baseline. Full results for FFHQ are presented in Table 2 of Section H.

Algorithm	Motion Blur		Gaussian Blur		SR $\times 4$		Inpainting		HDR		Phase Retrieval		NFE
	PSNR	lpips	PSNR	lpips	PSNR	lpips	PSNR	lpips	PSNR	lpips	PSNR	lpips	
DPIR	25.2	0.36	24.7	0.38	24.7	0.38	27.1	0.28	–	–	–	–	20
DPIR + ProxiMAP	25.4	0.37	25.0	0.38	24.7	0.38	27.3	0.27	–	–	–	–	160
DPIR + Fast ProxiMAP	25.5	0.36	25.0	0.38	24.8	0.38	27.9	0.26	–	–	–	–	27
DiffPIR	24.3	0.40	24.6	0.40	24.2	0.36	25.4	0.29	–	–	–	–	20
DiffPIR + ProxiMAP	25.1	0.37	24.9	0.36	23.3	0.38	25.7	0.28	–	–	–	–	160
DiffPIR + Fast ProxiMAP	25.2	0.34	25.1	0.35	24.8	0.36	25.6	0.28	–	–	–	–	27
DAPS	24.4	0.36	24.5	0.37	24.3	0.37	26.6	0.22	19.6	0.27	15.5	0.53	1200
DAPS + ProxiMAP	24.7	0.34	24.6	0.36	24.7	0.35	27.2	0.18	19.1	0.28	17.1	0.49	1200
PnPFlow	23.7	0.43	24.4	0.40	24.4	0.40	28.3	0.19	17.8	0.28	15.2	0.54	500
REDDiff	24.0	0.42	24.4	0.40	24.4	0.39	27.0	0.22	18.0	0.29	14.8	0.60	1000
SITCOM	24.6	0.35	24.9	0.37	25.0	0.33	26.1	0.27	17.8	0.34	14.6	0.55	800
DPS	23.7	0.32	23.7	0.30	24.2	0.33	27.0	0.21	19.4	0.24	13.5	0.59	2000

MMSE denoisers, it consistently sharpens reconstructions across multiple inverse problems, datasets, and noise levels. A hybrid variant that applies ProxiMAP only in the late iterations of PnP matches or exceeds the full-replacement variant at a fraction of the cost.

Broader impact. ProxiMAP improves the perceptual quality of reconstructions produced by Plug-and-Play methods across a range of inverse problems. Because the underlying diffusion models are pretrained on natural-image datasets, reconstructions inherit the biases and content distribution of those datasets; this is a property of the diffusion priors used rather than of ProxiMAP itself. More fundamentally, our analysis (Section 3.1) shows that diffusion-based MAP estimators recover what is most likely under the *learned* distribution rather than under the data distribution. This caveat is particularly relevant for safety-critical applications such as medical or scientific imaging, where downstream decisions should not rely on visual plausibility alone.

Acknowledgements

This work was supported by the ERC grant number 101087696 (APHELAIA project) and by the ANR project BONSAI (grant ANR-23-CE23-0012-01).

References

- Michael Samuel Albergo and Eric Vanden-Eijnden. Building normalizing flows with stochastic interpolants. In *International Conference on Learning Representations (ICLR)*, 2023.
- Ismail Alkhouri, Shijun Linag, Cheng-Han Huang, Jimmy Dai, Qing Qu, Saiprasad Ravishankar, and Rongrong Wang. SITCOM: Step-wise triple-consistent diffusion sampling for inverse problems. In *International Conference on Machine Learning (ICML)*, 2025.
- Giulio Biroli, Tony Bonnaire, Valentin De Bortoli, and Marc Mézard. Dynamical regimes of diffusion models. *Nature Communications*, 15(1):9957, 2024.
- Yochai Blau and Tomer Michaeli. The perception-distortion tradeoff. In *Conference on Computer Vision and Pattern Recognition (CVPR)*, 2018.
- Benjamin Boys, Mark Girolami, Jakiw Pidstrigach, Sebastian Reich, Alan Mosca, and O. Deniz Akyildiz. Tweedie moment projected diffusions for inverse problems. *Transactions on Machine Learning Research (TMLR)*, 2025.
- Stanley H Chan, Xiran Wang, and Omar A Elgendy. Plug-and-play admm for image restoration: Fixed-point convergence and applications. *IEEE Transactions on Computational Imaging*, 3(1): 84–98, 2016.
- Ricky TQ Chen, Yulia Rubanova, Jesse Bettencourt, and David K Duvenaud. Neural ordinary differential equations. *Adv. Neural Information Processing Systems (NeurIPS)*, 2018.
- Jooyoung Choi, Sungwon Kim, Yonghyun Jeong, Youngjune Gwon, and Sungroh Yoon. ILVR: Conditioning method for denoising diffusion probabilistic models. In *International Conference on Computer Vision (ICCV)*, 2021.
- Hyungjin Chung, Jeongsol Kim, Michael Thompson Mccann, Marc Louis Klasky, and Jong Chul Ye. Diffusion posterior sampling for general noisy inverse problems. In *International Conference on Learning Representations (ICLR)*, 2023.
- Patrick L. Combettes and Jean-Christophe Pesquet. *Proximal Splitting Methods in Signal Processing*, pages 185–212. 2011.
- Kostadin Dabov, Alessandro Foi, Vladimir Katkovnik, and Karen Egiazarian. Image denoising by sparse 3-D transform-domain collaborative filtering. *IEEE Trans. Image Process.*, 16(8):2080–2095, 2007.
- Mauricio Delbracio and Peyman Milanfar. Inversion by direct iteration: An alternative to denoising diffusion for image restoration. *Transactions on Machine Learning Research (TMLR)*, 2023.
- Jia Deng, Wei Dong, Richard Socher, Li-Jia Li, Kai Li, and Li Fei-Fei. ImageNet: A large-scale hierarchical image database. In *Conference on Computer Vision and Pattern Recognition (CVPR)*, 2009.
- Prafulla Dhariwal and Alexander Quinn Nichol. Diffusion models beat GANs on image synthesis. In *Adv. Neural Information Processing Systems (NeurIPS)*, 2021.
- Zhengan Fang, Sam Buchanan, and Jeremias Sulam. What’s in a prior? learned proximal networks for inverse problems. In *International Conference on Learning Representations (ICLR)*, 2024.

- Ruturaj G Gavaskar and Kunal N Chaudhury. Plug-and-play ista converges with kernel denoisers. *IEEE Signal Processing Letters*, 27:610–614, 2020.
- Alexandros Graikos, Nikolay Malkin, Nebojsa Jojic, and Dimitris Samaras. Diffusion models as plug-and-play priors. In Alice H. Oh, Alekh Agarwal, Danielle Belgrave, and Kyunghyun Cho, editors, *Adv. Neural Information Processing Systems (NeurIPS)*, 2022.
- Sai Bharath Chandra Gutha, Ricardo Vinuesa, and Hossein Azizpour. Inverse problems with diffusion models: A map estimation perspective. In *2025 IEEE/CVF Winter Conference on Applications of Computer Vision (WACV)*. IEEE, 2025a.
- Sai Bharath Chandra Gutha, Ricardo Vinuesa, and Hossein Azizpour. Inverse problems with diffusion models: MAP estimation via mode-seeking loss. In *arXiv:2512.10524*, 2025b.
- Samuel Hurault. *Convergent plug-and-play methods for image inverse problems with explicit and nonconvex deep regularization*. PhD thesis, Université de Bordeaux, 2023.
- Samuel Hurault, Arthur Leclaire, and Nicolas Papadakis. Proximal denoiser for convergent plug-and-play optimization with nonconvex regularization. In *International Conference on Machine Learning (ICML)*, 2022.
- Ajil Jalal, Marius Arvinte, Giannis Daras, Eric Price, Alexandros G Dimakis, and Jon Tamir. Robust compressed sensing mri with deep generative priors. In M. Ranzato, A. Beygelzimer, Y. Dauphin, P.S. Liang, and J. Wortman Vaughan, editors, *Adv. Neural Information Processing Systems (NeurIPS)*, 2021.
- Zahra Kadkhodaie and Eero P Simoncelli. Solving linear inverse problems using the prior implicit in a denoiser. *arXiv preprint arXiv:2007.13640*, 2020.
- Mason Kamb and Surya Ganguli. An analytic theory of creativity in convolutional diffusion models. In *International Conference on Machine Learning (ICML)*, 2025.
- Ulugbek S. Kamilov, Charles A. Bouman, Gregory T. Buzzard, and Brendt Wohlberg. Plug-and-play methods for integrating physical and learned models in computational imaging: Theory, algorithms, and applications. *IEEE Signal Processing Magazine*, 40(1):85–97, 2023.
- Rafal Karczewski, Markus Heinonen, and Vikas Garg. Diffusion models as cartoonists: The curious case of high density regions. In *International Conference on Learning Representations (ICLR)*, 2025.
- Tero Karras, Samuli Laine, and Timo Aila. A style-based generator architecture for generative adversarial networks. In *Conference on Computer Vision and Pattern Recognition (CVPR)*, 2019.
- Tero Karras, Miika Aittala, Timo Aila, and Samuli Laine. Elucidating the design space of diffusion-based generative models. In *Adv. Neural Information Processing Systems (NeurIPS)*, 2022.
- Rémi Laumont, Valentin De Bortoli, Andrés Almansa, Julie Delon, Alain Durmus, and Marcelo Pereyra. On maximum a posteriori estimation with plug & play priors and stochastic gradient descent. *Journal of Mathematical Imaging and Vision (JMIV)*, 65(1):140–163, 2023.
- Xin Li, Yulin Ren, Xin Jin, Cuiling Lan, Xingrui Wang, Wenjun Zeng, Xinchao Wang, and Zhibo Chen. Diffusion models for image restoration and enhancement: A comprehensive survey. *International Journal on Computer Vision (IJCV)*, 133(11):8078–8108, 2025.

- Xingchao Liu, Chengyue Gong, and Qiang Liu. Flow straight and fast: Learning to generate and transfer data with rectified flow. In *International Conference on Learning Representations (ICLR)*, 2023.
- Morteza Mardani, Jiaming Song, Jan Kautz, and Arash Vahdat. A variational perspective on solving inverse problems with diffusion models. In *International Conference on Learning Representations (ICLR)*, 2024.
- Ségolène Tiffany Martin, Anne Gagneux, Paul Hagemann, and Gabriele Steidl. PnP-Flow: Plug-and-play image restoration with flow matching. In *International Conference on Learning Representations (ICLR)*, 2025.
- T. Meinhardt, M. Moeller, C. Hazirbas, and D. Cremers. Learning proximal operators: Using denoising networks for regularizing inverse imaging problems. In *International Conference on Computer Vision (ICCV)*, 2017.
- Pravin Nair, Ruturaj G Gavaskar, and Kunal Narayan Chaudhury. Fixed-point and objective convergence of plug-and-play algorithms. *IEEE Transactions on Computational Imaging*, 7: 337–348, 2021.
- Miles Olson, Elizabeth Santorella, Louis C. Tiao, Sait Cakmak, Mia Garrard, Samuel Daulton, Zhiyuan Jerry Lin, Sebastian Ament, Bernard Beckerman, Eric Onofrey, Paschal Igusti, Cristian Lara, Benjamin Letham, Cesar Cardoso, Shiyun Sunny Shen, Andy Chenyuan Lin, Matthew Grange, Elena Kashtelyan, David Eriksson, Maximilian Balandat, and Eytan. Bakshy. Ax: A platform for adaptive experimentation. In *AutoML 2025*, 2025.
- Neal Parikh and Stephen Boyd. Proximal algorithms. *Foundations and Trends in optimization*, 1(3): 127–239, 2014.
- Scott Pesme, Giacomo Meanti, Michael Arbel, and Julien Mairal. MAP estimation with denoisers: Convergence rates and guarantees. In *Adv. Neural Information Processing Systems (NeurIPS)*, 2025.
- Marien Renaud, Jean Prost, Arthur Leclaire, and Nicolas Papadakis. Plug-and-play image restoration with stochastic denoising regularization. In *International Conference on Machine Learning (ICML)*, 2024.
- Yaniv Romano, Michael Elad, and Peyman Milanfar. The little engine that could: Regularization by denoising (RED). *SIAM Journal on Imaging Sciences*, 10(4):1804–1844, 2017.
- Christopher Scovelis, Haitz Sáez de Ocáriz Borde, and Justin Solomon. Closed-form diffusion models. *Transactions on Machine Learning Research (TMLR)*, 2025.
- Jiaming Song, Chenlin Meng, and Stefano Ermon. Denoising diffusion implicit models. In *International Conference on Learning Representations (ICLR)*, 2021a.
- Yang Song, Jascha Sohl-Dickstein, Diederik P Kingma, Abhishek Kumar, Stefano Ermon, and Ben Poole. Score-based generative modeling through stochastic differential equations. In *International Conference on Learning Representations (ICLR)*, 2021b.
- Suhas Sreehari, S. V. Venkatakrisnan, Brendt Wohlberg, Gregory T. Buzzard, Lawrence F. Drummy, Jeffrey P. Simmons, and Charles A. Bouman. Plug-and-play priors for bright field electron

- tomography and sparse interpolation. *IEEE Transactions on Computational Imaging*, 2(4): 408–423, 2016.
- Matthieu Terris, Audrey Repetti, Jean-Christophe Pesquet, and Yves Wiaux. Building firmly nonexpansive convolutional neural networks. In *IEEE International Conference on Acoustics, Speech and Signal Processing (ICASSP)*, 2020.
- Singanallur V. Venkatakrishnan, Charles A. Bouman, and Brendt Wohlberg. Plug-and-play priors for model based reconstruction. In *IEEE Global Conference on Signal and Information Processing*, 2013.
- Xiaojian Xu, Yu Sun, Jiaming Liu, Brendt Wohlberg, and Ulugbek S Kamilov. Provable convergence of plug-and-play priors with mmse denoisers. *IEEE Signal Processing Letters*, 27:1280–1284, 2020.
- TaeHo Yoon, Joo Young Choi, Sehyun Kwon, and Ernest K Ryu. Diffusion probabilistic models generalize when they fail to memorize. In *International Conference on Machine Learning (ICML) 2023 workshop on structured probabilistic inference & generative modeling*, 2023.
- Bingliang Zhang, Wenda Chu, Julius Berner, Chenlin Meng, Anima Anandkumar, and Yang Song. Improving diffusion inverse problem solving with decoupled noise annealing. In *Conference on Computer Vision and Pattern Recognition (CVPR)*, 2025a.
- Kai Zhang, Wangmeng Zuo, Shuhang Gu, and Lei Zhang. Learning deep CNN denoiser prior for image restoration. In *Conference on Computer Vision and Pattern Recognition (CVPR)*, 2017.
- Kai Zhang, Yawei Li, Wangmeng Zuo, Lei Zhang, Luc Van Gool, and Radu Timofte. Plug-and-play image restoration with deep denoiser prior. *IEEE Transactions on Pattern Analysis and Machine Intelligence*, 44(10):6360–6376, 2021.
- Shaorong Zhang, Rob Brekelmans, and Greg Ver Steeg. Local MAP sampling for diffusion models. In *arXiv preprint arXiv:2510.07343*, 2025b. arXiv:2510.07343.
- Yuanzhi Zhu, Kai Zhang, Jingyun Liang, Jiezhong Cao, Bihan Wen, Radu Timofte, and Luc Van Gool. Denoising diffusion models for plug-and-play image restoration. In *Conference on Computer Vision and Pattern Recognition (CVPR) Workshop*, 2023.

A A Discussion on MAP Estimation

Section 3.1 established two facts that deserve unpacking. First, MAP-targeting with the schedule of Pesme et al. (2025) fails on diffusion models trained on natural images, even though the same schedule succeeds with the exact score of a Gaussian mixture model. Second, this failure is driven by the implicit biases of diffusion model training displacing the modes of the learned distribution away from those of the data distribution. We discuss here what this means for MAP estimation under learned priors more broadly, and the precise sense in which ProxiMAP acts as principled early stopping.

The status of MAP under learned priors. The diagnosis is a statement about the *learned* posterior, not about MAP estimation itself. The conditional log-likelihood values reported in Fig. 2 are unambiguous: cartoon outputs are the legitimate maximizers of $\log p_\theta(x | y)$ where p_θ is the distribution implied by the learned score. They are also visually unrealistic. The reconciliation is that p_θ is not the data distribution. The implicit biases that allow diffusion models to generalize beyond the training set Kamb and Ganguli (2025); Scarvelis et al. (2025); Yoon et al. (2023) also smooth and reshape the high-density regions in ways that do not preserve typicality. As a corollary, the MAP of the data distribution—which we cannot access—and the MAP of the learned distribution—which we can in principle compute—are different objects, and targeting the latter is not what one wants. Our results suggest a tension between generalization and MAP-faithfulness in diffusion-based priors: Section B confirms this from the other direction, showing that a diffusion model trained in the memorizing regime Biroli et al. (2024)—where the implicit smoothing is suppressed—produces artifact-free MAP estimates from (5).

Connections and outlook. The cartoon effect we exploit here was studied in its own right by Karczewski et al. (2025) as a property of high-density regions of pretrained diffusion models. Our contribution is methodological: identifying it as the operative obstacle to PnP-style MAP estimation, and showing that the noise-matching constraint avoids it.

A clear caveat is that ProxiMAP does not converge to a well-defined fixed point. Its sharpness and faithfulness come from stopping in the regime where the learned score remains reliable, which is a property of the schedule rather than of any limit of the iteration. Whether a notion of MAP can be formulated for learned image priors that is both well-defined and aligned with perceptual quality remains open—perhaps via priors trained explicitly to align their high-density regions with the data manifold, or via posterior objectives less sensitive to the implicit smoothing of standard diffusion training. In the meantime, our results indicate that the most useful design lever is the iterate’s relationship to the regime where the learned score is reliable: by managing this relationship explicitly, schedule-based methods can extract sharp, faithful reconstructions from existing diffusion models without requiring any change to how those models are trained.

B Memorization in Diffusion Models

We train two flow-matching models on the CIFAR10 dataset. The first – the *generalizing model* – is trained on the full training set of 50000 images, the second – the *memorizing model* – is trained on only 5000 images. Both models have the same number of parameters. We observe that the two training losses follow a similar trajectory in the early stages of training, until a certain point after which the training loss of the memorizing model rapidly decreases. The model thus enters the *memorizing regime* (Biroli et al., 2024) in which it is unable to generate novel samples and

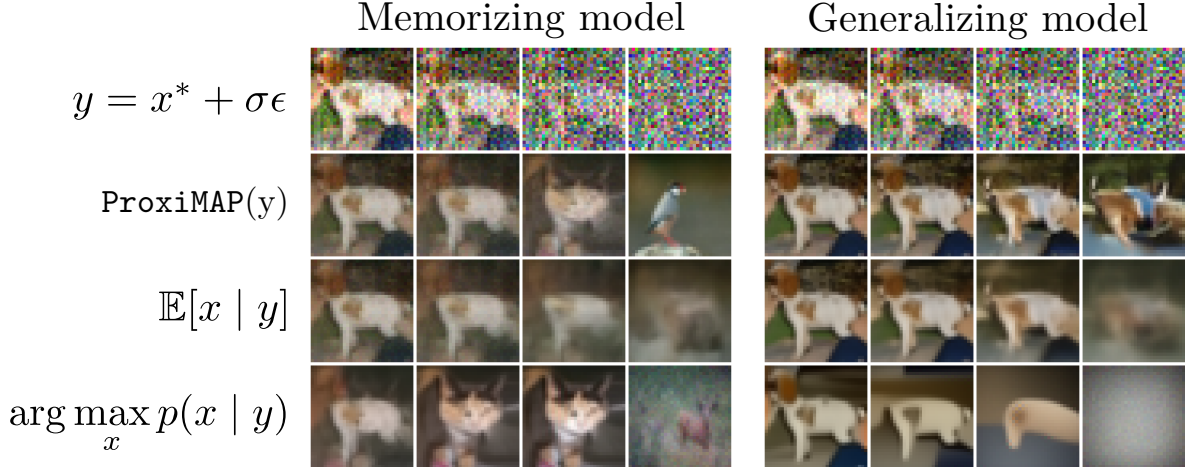


Figure 7: Comparing the conditional performance of a memorizing and a generalizing diffusion model. The rows correspond to a) the conditioning variable (which shows increasing amounts of noise from left to right), b) images obtained with ProxiMAP, c) the MMSE estimate and d) the MAP obtained via Eq. (5).

will replicate ones from the training set. We test both models on two smoothed GD schedules: the theoretically supported one of Eq. (5) (proposed by Pesme et al. (2025)) and the *early-stopped* one proposed here. Referencing Fig. 7, for the generalizing model, we observe a similar effect to what we reported in Section A: the MAP estimation needs to be early-stopped to prevent ending into the *cartoon region*. This however does not happen for the memorizing model. As the flow-matching network learns to replicate its training samples its score becomes more accurate and the fast, non-early-stopped algorithm of Pesme et al. (2025) generates clean, realistic images. Of course, this does not mean that we should use a memorizing model: while it generates realistic images, these will always come from the training set - rendering it useless for any task which involves unseen samples.

C Behaviour of the Recursive Noise Sequence $(\sigma_k)_k$

Consider the recursive sequence defined by

$$\sigma_{k+1} = (1 - \beta)\sigma_k + \frac{\beta\sigma_0}{1 + \frac{\tau}{\sigma_k^2}} \quad (8)$$

with parameters $\beta \in (0, 1)$, $\tau > 0$, $\sigma_0 > 0$, and initialisation $\sigma_{k=0} = \sigma_0$.

Lemma 1. *Let $(\sigma_k)_{k \geq 0}$ be the sequence defined by (8). Then $\sigma_k \rightarrow 0$ as $k \rightarrow \infty$ if and only if*

$$\tau > \frac{\sigma_0^2}{4}.$$

Proof. Define the map $f : (0, \infty) \rightarrow (0, \infty)$ by

$$f(\sigma) = (1 - \beta)\sigma + \frac{\beta\sigma_0}{1 + \tau/\sigma^2} = (1 - \beta)\sigma + \frac{\beta\sigma_0\sigma^2}{\sigma^2 + \tau},$$

such that $\sigma_{k+1} = f(\sigma_k)$. Note that $f(\sigma) > 0$ for all $\sigma > 0$, so the sequence stays positive. Moreover, f extends continuously to $\sigma = 0$ with $f(0) = 0$, so $\sigma = 0$ is always a fixed point. Concerning potential other fixed points, notice that a positive fixed point satisfies $f(\sigma) = \sigma$, i.e.

$$(1 - \beta)\sigma + \frac{\beta\sigma_0\sigma^2}{\sigma^2 + \tau} = \sigma.$$

Subtracting $(1 - \beta)\sigma$ from both sides and dividing by $\beta\sigma > 0$ gives

$$\frac{\sigma_0\sigma}{\sigma^2 + \tau} = 1 \implies \sigma^2 - \sigma_0\sigma + \tau = 0.$$

The discriminant of this quadratic is $\sigma_0^2 - 4\tau$ and real solutions exist if and only if $\tau \leq \sigma_0^2/4$ and the fixed points are then

$$\sigma_{\pm} = \frac{\sigma_0 \pm \sqrt{\sigma_0^2 - 4\tau}}{2} > 0.$$

We now split the proof into the two directions.

Sufficient condition: $\tau > \sigma_0^2/4 \implies \sigma_k \rightarrow 0$. When $\tau > \sigma_0^2/4$, then f has only 0 as a fixed point. We now show $f(\sigma) < \sigma$ for all $\sigma > 0$, so (σ_k) is strictly decreasing.

$$\begin{aligned} f(\sigma) < \sigma &\iff (1 - \beta)\sigma + \frac{\beta\sigma_0\sigma^2}{\sigma^2 + \tau} < \sigma \\ &\iff \frac{\beta\sigma_0\sigma^2}{\sigma^2 + \tau} < \beta\sigma \\ &\iff \frac{\sigma_0\sigma}{\sigma^2 + \tau} < 1 \\ &\iff \sigma^2 - \sigma_0\sigma + \tau > 0. \end{aligned}$$

The last inequality is true for all σ if $\tau > \sigma_0^2/4$. Hence (σ_k) is strictly decreasing and bounded below by 0, so it converges to some limit $\ell \geq 0$. Taking $k \rightarrow \infty$ in the recursion $\sigma_{k+1} = f(\sigma_k)$ yields $\ell = f(\ell)$, so ℓ is a fixed point of f in $[0, \infty)$. Since the only such fixed point is 0, we conclude $\sigma_k \rightarrow 0$.

Necessary condition: $\tau \leq \sigma_0^2/4$, then $\sigma_k \not\rightarrow 0$. If $\tau \leq \sigma_0^2/4$, then the largest fixed point $\sigma_+ = \frac{\sigma_0 + \sqrt{\sigma_0^2 - 4\tau}}{2} > 0$ is strictly smaller than σ_0 , which means that the initialisation $\sigma_{k=0}$ is larger than any fixed point. Now recall that

$$f(\sigma) < \sigma \iff \sigma^2 - \sigma_0\sigma + \tau > 0.$$

Which means that $f(\sigma) < \sigma$ for $\sigma > \sigma_+$. Also a simple analysis of the function f shows that it is increasing over $\mathbb{R}_{\geq 0}$. Putting things together, if $\sigma_+ \leq \sigma_k$, then

$$\sigma_+ = f(\sigma_+) \leq \sigma_{k+1} = f(\sigma_k) \leq \sigma_k.$$

Since $\sigma_{k=0} = \sigma_0 > \sigma_+$, we have that σ_k is a decreasing function lower-bounded by σ_+ . It follows that it must converge towards some limit $\ell \geq \sigma_+$ such that $f(\ell) = \ell$. Hence $\ell = \sigma_+ \neq 0$ which concludes the proof. \square

D Details about PnP Algorithms

Algorithms 2 to 4 provide more precise pseudo-code of the algorithms we used in this work. For DPIP and DiffPIP, we simply plugged ProxiMAP in-place of the denoiser D_θ . For DAPS we also changed the outer-loop noise schedule (which in the original paper is the EDM (Karras et al., 2022) schedule) to follow the ProxiMAP schedule. The resulting iterative algorithm is presented in Algorithm 5.

Algorithm 2 DPIR

Require: data-fidelity f , denoiser D_θ , y , σ_y , K **Require:** hyperparameters σ_{\max} , γ 1: $(\sigma_k)_{k=0}^{K-1} \leftarrow \text{logspace}(\log(\sigma_{\max}), \log(\sigma_y), K)$ 2: $x_0 \leftarrow \mathcal{A}^\top y$ 3: **for** $k = 0, \dots, K - 1$ **do**4: $\gamma_k \leftarrow \gamma \left(\frac{\sigma_k}{\sigma_y} \right)^2$ 5: $z \leftarrow \text{prox}_{\gamma_k f}(x_k)$ 6: $x_{k+1} \leftarrow D_\theta(z, \sigma_k)$ \triangleright Replace this with a call to ProxiMAP7: **end for**8: **return** x_K

Algorithm 3 DiffPIR

Require: data-fidelity f , denoiser D_θ , y , σ_y , K **Require:** hyperparameters ζ , λ **Require:** DDIM schedule $(\bar{\alpha}_k)_{k=1}^K$ 1: $x_0 \sim \mathcal{N}(0, \sigma_0)$ \triangleright More refined initialization in practice2: **for** $k = 0, \dots, K - 1$ **do**3: $\rho_k \leftarrow \lambda \sigma_y^2 \left(\frac{\sqrt{\bar{\alpha}_k}}{\sqrt{1 - \bar{\alpha}_k}} \right)^2$ 4: $\hat{x}_{\text{MMSE}} \leftarrow D_\theta \left(\frac{x_k}{\sqrt{\bar{\alpha}_k}}, \frac{\sqrt{1 - \bar{\alpha}_k}}{\sqrt{\bar{\alpha}_k}} \right)$ \triangleright Replace this with a call to ProxiMAP5: $\hat{x} \leftarrow \text{prox}_{\frac{\rho_k}{f}}(\hat{x}_{\text{MMSE}})$ 6: $\hat{\epsilon} \leftarrow \frac{x_k - \sqrt{\bar{\alpha}_k} \hat{x}_{\text{MMSE}}}{\sqrt{1 - \bar{\alpha}_k}}$ 7: $\epsilon \sim \mathcal{N}(0, \sqrt{1 - \bar{\alpha}_k} I)$ 8: $x_{k+1} \leftarrow \sqrt{\bar{\alpha}_k} \hat{x} + \sqrt{1 - \bar{\alpha}_k} (\sqrt{1 - \zeta} \hat{\epsilon} + \sqrt{\zeta} \epsilon)$ 9: **end for**10: **return** \hat{x}_{MMSE}

Algorithm 4 DAPS

Require: data-fidelity f , denoiser D_θ , y , σ_y , K , J **Require:** hyperparameters γ_{init} **Require:** EDM schedule $(\sigma_k)_{k=1}^K$ 1: $\gamma_{\min} \leftarrow 0.01$ 2: $x_0 \sim \mathcal{N}(0, \sigma_{\max})$ 3: **for** $k = 0, \dots, K - 1$ **do**4: $\hat{x}_{\text{sample}} \sim p_0(X | X_{\sigma_k} = x_k, D_\theta)$ \triangleright PF-ODE sampling (EDM schedule, Euler solver)5: $z_0 \leftarrow \hat{x}_{\text{sample}}$ 6: $\gamma_k \leftarrow \gamma_{\text{init}} \left(1 + \frac{k}{K} (\gamma_{\min} - 1) \right)$ 7: **for** $j = 0, \dots, J - 1$ **do** \triangleright Langevin sampling8: $\epsilon \sim \mathcal{N}(0, I)$ 9: $z_{j+1} \leftarrow z_j - \gamma_k \left(\nabla f(z_j, y) + \frac{z_j - z_0}{\sigma_k^2} \right) + \sqrt{2\gamma_k} \epsilon$ 10: **end for**11: $x_{k+1} \leftarrow z_J + \mathcal{N}(0, \sigma_{k+1} I)$ 12: **end for**13: **return** z_J

Algorithm 5 DAPS+ProxiMAP

Require: data-fidelity f , denoiser $D_\theta, y, \sigma_y, K, J$

Require: hyperparameters $\gamma_{\text{init}}, \sigma_{\text{final}}$

Require: ProxiMAP schedule $(\sigma_k)_{k=1}^K$

```
1:  $\gamma_{\text{min}} \leftarrow 0.01$ 
2:  $x_0 \sim \mathcal{N}(0, \sigma_{\text{max}})$ 
3: for  $k = 0, \dots, K - 1$  do
4:    $\hat{x}_{\text{ProxiMAP}} \leftarrow \text{ProxiMAP}(x_k, \sigma_k, D_\theta)$ 
5:    $z_0 \leftarrow \hat{x}_{\text{ProxiMAP}}$ 
6:    $\gamma_k \leftarrow \gamma_{\text{init}} \left(1 + \frac{k}{K}(\gamma_{\text{min}} - 1)\right)$ 
7:   for  $j = 0, \dots, J - 1$  do ▷ Langevin sampling
8:      $\epsilon \sim \mathcal{N}(0, I)$ 
9:      $z_{j+1} \leftarrow z_j - \gamma_k \left(\nabla f(z_j, y) + \frac{z_j - z_0}{\sigma_k^2}\right) + \sqrt{2\gamma_k}\epsilon$ 
10:  end for
11:   $x_{k+1} \leftarrow z_J + \mathcal{N}(0, \sigma_{k+1}I)$ 
12: end for
13: return  $z_J$ 
```

E Denoising Experimental Details

For the denoising experiment of Fig. 4, we used the full testing datasets at our disposal (100 images for FFHQ, 100 for ImageNet). The task was simply to remove additive Gaussian noise with increasing variance from each test image. We set σ_{final} to 0.005 for ProxiMAP for all runs. The other algorithms (InDI, DDIM, Flow-matching) were similarly not tuned further. We used PSNR and LPIPS as metrics to highlight the perception-distortion tradeoff. In particular – throughout the paper – LPIPS was computed with the VGG-16 network. In the main text we showed the ImageNet results. In Fig. 8 we show the results on FFHQ. The conclusions are the same between the two datasets: while all compared algorithms perform similarly, ProxiMAP converges with fewer iterations to good solutions dominating the competing methods.

F Description of the Tasks

We describe in more detail the inverse problems on which we ran evaluations in the paper. The first 5 are linear problems, for which the prox of the data-fidelity term can be computed easily. The last two instead are non-linear and do not have a closed-form proximal operator. For this reason we did not test DPIR and DiffPIR (which require the proximal operator of the data-fidelity term) on the non-linear tasks. All tasks apart from block inpainting were run with levels $\sigma = 0.05$ with additive Gaussian noise applied to the corrupted images in the $[0, 1]$ range. Block inpainting was only considered in the noiseless setting, since in practice it is more related to image editing of high-quality images rather than image restoration.

- **Gaussian blur.** We used a kernel of size 61x61, with a standard deviation of 3 and *circular* padding.
- **Motion blur.** We used a standard kernel generating function with kernel size 61x61 and intensity of 0.5. Once again with circular padding.
- **Superresolution.** $\times 4$ decimation preceded by a bicubic filter, circular padding.

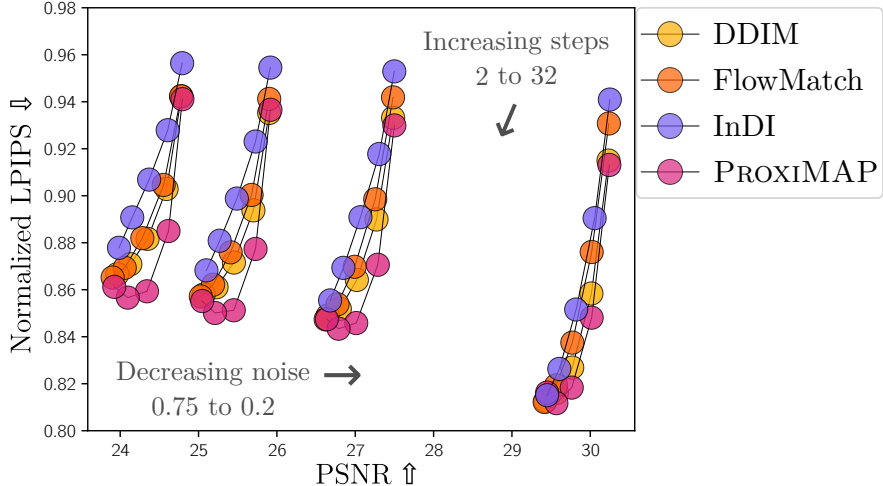


Figure 8: FFHQ Gaussian denoising results. LPIPS is normalized such that the MMSE denoiser has an LPIPS of 1.

- **Random inpainting.** Masked 70% of pixels setting them to the intermediate range value (0.5).
- **High dynamic range.** A non-linear forward model consisting of multiplying all pixel values by 2 and clamping them to lie within the $[0, 1]$ range.
- **Phase retrieval.** A second non-linear task. Consists of recovering phase information from only the real-valued part of the image’s FFT. This forward model is invariant to vertical flips of the image – and hence the recovered image may occasionally be flipped. To correctly compute reconstruction metrics for this task we evaluated them on both the original image and the flipped image, picking the metrics with the highest PSNR among the two.

G PnP Experiment Details

To run the plug-and-play experiment, for which results are reported in Fig. 6 and Table 1, we re-implemented and ran the competing algorithms in order to allocate fair amounts of hyperparameter tuning effort. The hyperparameters and their tuning ranges are described below. Note that the hyperparameters ranges for ProxiMAP and for Fast ProxiMAP were kept the same.

- **DPIR.** We fixed the number of iterations to 20 and performed hyperparameter tuning by sweeping over two additional control knobs. The first one controls the schedule of decreasing noise levels with which the denoiser is called. The maximum noise level was swept between $[0.001, 100]$ considering that the original paper set it to 0.2 (but with a different denoising model). The second controls the weight given to the data-fidelity term. It was originally set to approximately 5 and we swept it over the range $[0.1, 40]$.
- **DPIR+ProxiMAP.** We fixed the number of ProxiMAP iterations to 8 and additionally swept the σ_{final} parameter between $[0.001, 0.2]$.
- **DiffPIR.** We fixed the number of iterations to 20 since – while not the best performance possible – it reaches fairly good results with minimal computation time. We swept λ over $[0.1, 30]$ and ζ over $[0, 1]$.

- **DiffPIR+ProxiMAP.** We fixed the number of **ProxiMAP** iterations to 8 and additionally swept the σ_{final} parameter between $[0.001, 0.2]$.
- **DAPS.** We fixed the number of Langevin steps (data-fidelity optimization) to 50, the number of outer iterations to 200 and the number of ODE sampling (inner) iterations to 6. We swept over the Langevin learning-rate parameter (which controls the strength of the data-fidelity term) between $[0.000001, 0.0002]$.
- **DAPS+ProxiMAP.** In addition to **DAPS** we swept over the σ_{final} parameter for the inner **ProxiMAP** iteration between $[0.001, 0.2]$. We fixed the outer **ProxiMAP** schedule to have $\sigma_{\text{final}} = 0.1$ which is close to the final noise-level in **DDIM** for 200 steps.
- **PnPFlow.** We adapted the algorithm to work with **DDPM**-based models instead of flow-matching. We used 500 iterations, and did not perform averaging over multiple samples as we did not find it to significantly improve performance. We swept over the learning-rate parameter α between $[0.001, 0.9]$.
- **REDDiff.** We fixed the number of steps to 1000. We swept the overall learning rate over $[0.001, 0.5]$ and the weight of the regularization term between $[0.01, 10]$, while the data-fidelity weight was fixed to 1.
- **SITCOM.** We fixed the number of annealing iterations to 20 and of inversion iterations to 20. We swept the learning rate of the model inversion over $[0.001, 0.1]$ and $\delta \in [0.001, 0.1]$ which controls a threshold on the loss for early stopping.
- **DPS.** We fixed the number of iterations to 1000, varied $\zeta \in [0, 1]$ (this is the noise parameter which interpolates between **DDPM** and **DDIM**), and swept over the data-fidelity gradient’s strength between $[0.1, 12]$.

In Table 2 (which complements Table 1 in the main text) we compare all the algorithms we considered on different inverse problems for noise-levels 0.05 on the FFHQ dataset. Note for both tables we took the configuration among the ones used for testing (which were chosen because of good hyperparameters on the validation set) with the minimum LPIPS. This is an arbitrary choice in order to present tabular-form results.

H Additional Results for PnP Experiments

First, the results of fully replacing the MMSE denoiser with **ProxiMAP** in PnP algorithms are detailed in Table 2 and Fig. 9. **DPIR+ProxiMAP** is a slight improvement on ImageNet, but is not as consistent on FFHQ—a discrepancy we attribute to **DPIR**’s schedule, which does not match the residual noise of its iterates. The MMSE denoiser is robust to this mismatch; **ProxiMAP**, by design (Section 3.2), is not. The hybrid variant introduced in Section 4.2 solves this issue.

To optimize the balance between computational efficiency and restoration quality, we further investigate this hybrid **ProxiMAP** approach. To reduce the overall number of function evaluations (NFEs), our strategy utilizes the MMSE denoiser during the initial iterations—when noise levels are high and coarse approximations are sufficient—before transitioning to **ProxiMAP** for final refinement. Crucially, this directly circumvents the noise schedule mismatch in **DPIR**; it leverages the robust MMSE denoiser precisely during the stages where **ProxiMAP** is most susceptible to severe performance degradation. We hypothesized that this transition could occur late in the process, as high-fidelity refinement is unnecessary during the early stages. An analysis of the Pareto fronts across various

Table 2: FFHQ, $\sigma_y = 0.05$. (Same as Table 1 but on FFHQ). We pick the HP sample from the Pareto front with the lowest LPIPS. Empty cells: DPIR and DiffPIR require a closed-form proximal step and so do not apply to non-linear tasks. NFEs are doubled for methods requiring backward passes. Colors indicate whether the ProxiMAP variant is **better than** or **worse than** the corresponding baseline.

Algorithm	Motion Blur		Gaussian Blur		SR $\times 4$		Inpainting		HDR		Phase Retrieval		NFE
	PSNR	lpips	PSNR	lpips	PSNR	lpips	PSNR	lpips	PSNR	lpips	PSNR	lpips	
DPIR	26.96	0.321	27.52	0.331	26.96	0.336	29.81	0.240	–	–	–	–	20
DPIR + ProxiMAP	26.54	0.281	25.05	0.289	24.91	0.300	27.80	0.228	–	–	–	–	160
DPIR + Fast ProxiMAP	27.74	0.260	28.70	0.252	28.16	0.266	31.76	0.185	–	–	–	–	27
DiffPIR	27.42	0.227	28.10	0.269	26.79	0.241	28.85	0.200	–	–	–	–	20
DiffPIR + ProxiMAP	27.49	0.236	27.33	0.210	26.86	0.225	28.28	0.183	–	–	–	–	160
DiffPIR + Fast ProxiMAP	28.37	0.235	28.75	0.246	28.18	0.253	28.90	0.200	–	–	–	–	27
DAPS	27.51	0.242	28.04	0.239	27.46	0.247	29.84	0.181	22.09	0.197	24.13	0.309	1200
DAPS + ProxiMAP	27.74	0.233	28.24	0.236	27.29	0.242	31.91	0.132	22.19	0.171	26.22	0.261	1200
PnPFlow	27.10	0.298	28.24	0.281	27.79	0.286	31.77	0.139	20.51	0.188	23.83	0.306	500
REDDiff	26.54	0.291	28.08	0.274	27.83	0.286	30.47	0.168	20.77	0.207	16.47	0.485	1000
SITCOM	27.52	0.267	28.18	0.261	28.10	0.245	28.66	0.220	23.31	0.214	23.01	0.327	800
DPS	26.42	0.223	27.06	0.202	27.00	0.219	30.40	0.142	22.64	0.169	20.94	0.358	2000

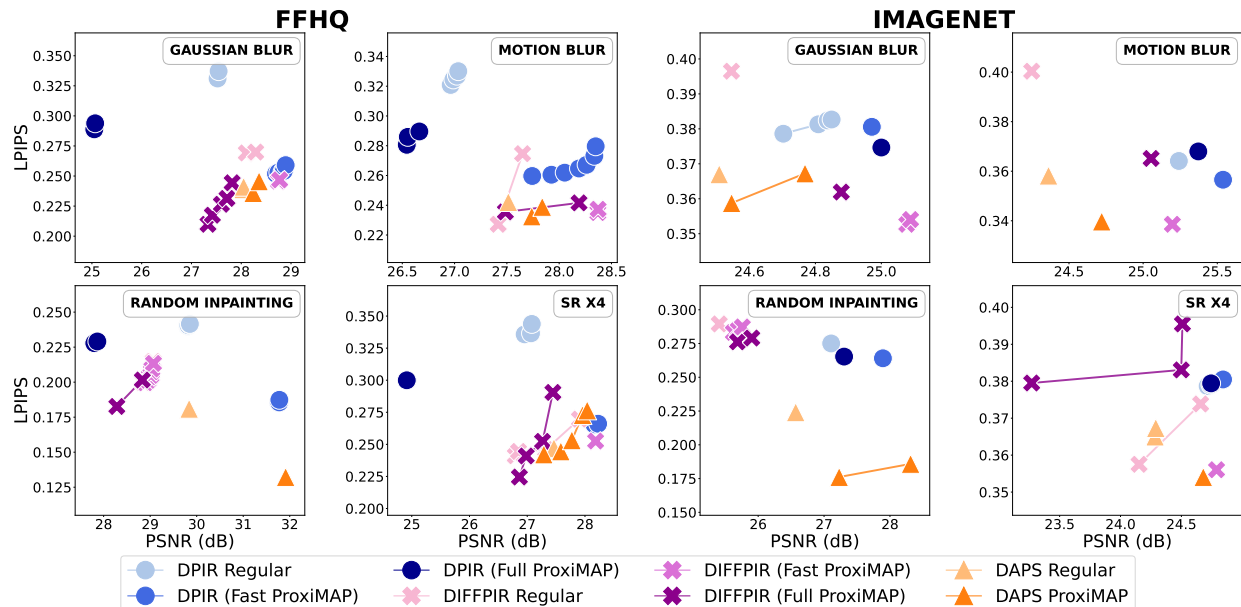


Figure 9: Baseline algorithms versus their full-replacement ProxiMAP counterparts and their fast ProxiMAP counterparts on four inverse problems at $\sigma_y = 0.05$. Lighter colors are baselines; darkest colors are full-replacement ProxiMAP and intermediate colors are fast ProxiMAP variants.

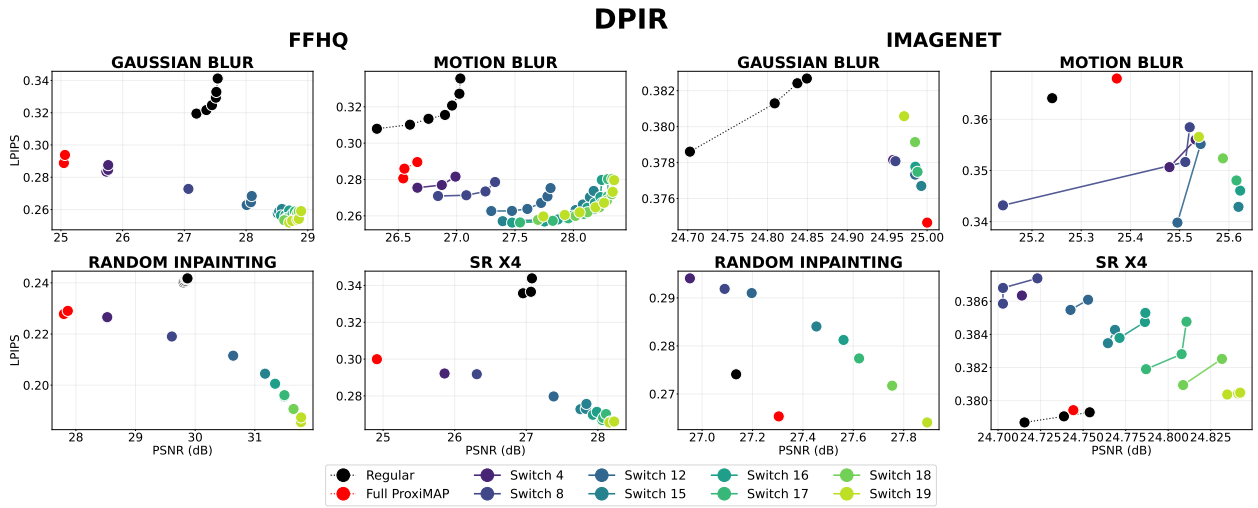


Figure 10: Trade-off between precision and computation cost for many hybrid variants of DPIR.

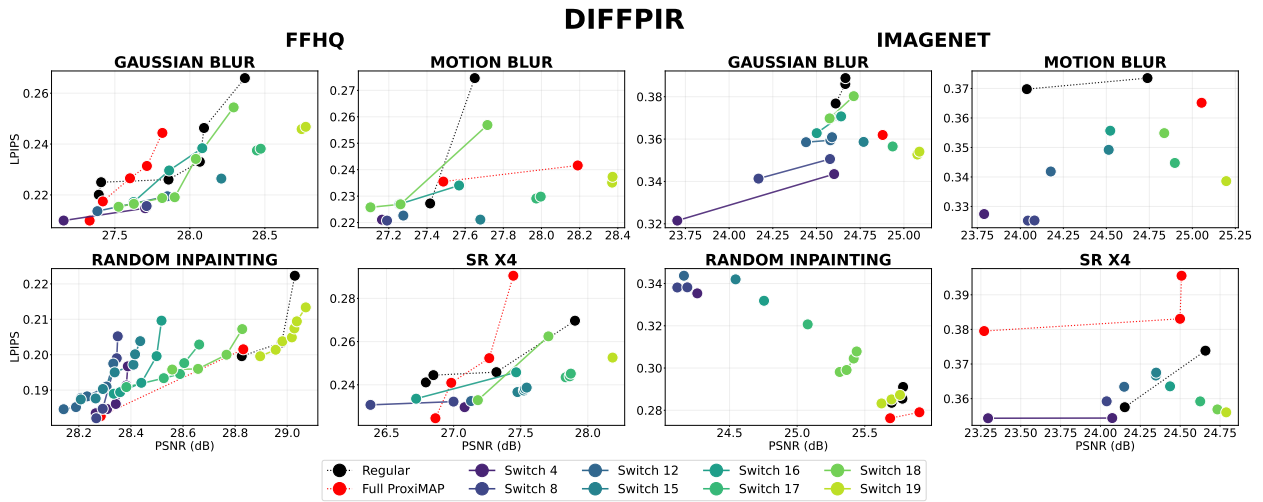


Figure 11: Same as Fig. 10, but on DiffPIR

switch steps confirms this intuition. Interestingly, delaying the switch until step 19 yielded optimal results for D_{PIR}, a remarkably late transition given that step 20 corresponds to the baseline standard PnP. While this optimal peak at step 19 is less pronounced for Diff_{PIR} (particularly on FFHQ), we adopt it uniformly; it maintains an improvement over the full-replacement baseline while maximizing computational efficiency. These performance trade-offs are illustrated in Figs. 10 and 11, with corresponding qualitative results provided in Figs. 12 to 15.

Failure cases and how Fast ProxiMAP resolves them The hyperparameter search did not always converge to good configurations within the allotted budget for D_{PIR}+ProxiMAP. This issue occurred for the super-resolution task on FFHQ, where Fig. 16 shows high-frequency artifacts along image edges in a few images produced by D_{PIR}+ProxiMAP. These artifacts have a characteristic appearance reminiscent of the early stages of the cartoon effect produced by the iteration of Eq. (5) (Section 3.1). Fast ProxiMAP resolves this issue cleanly, as visible in the same figure: by relying on the standard MMSE denoiser for the early iterations, the hybrid variant avoids entering the regime where score errors generate artifacts, while still benefiting from ProxiMAP’s sharpening in the late iterations. This is consistent with the noise-matching design analysis of Section 3.2.

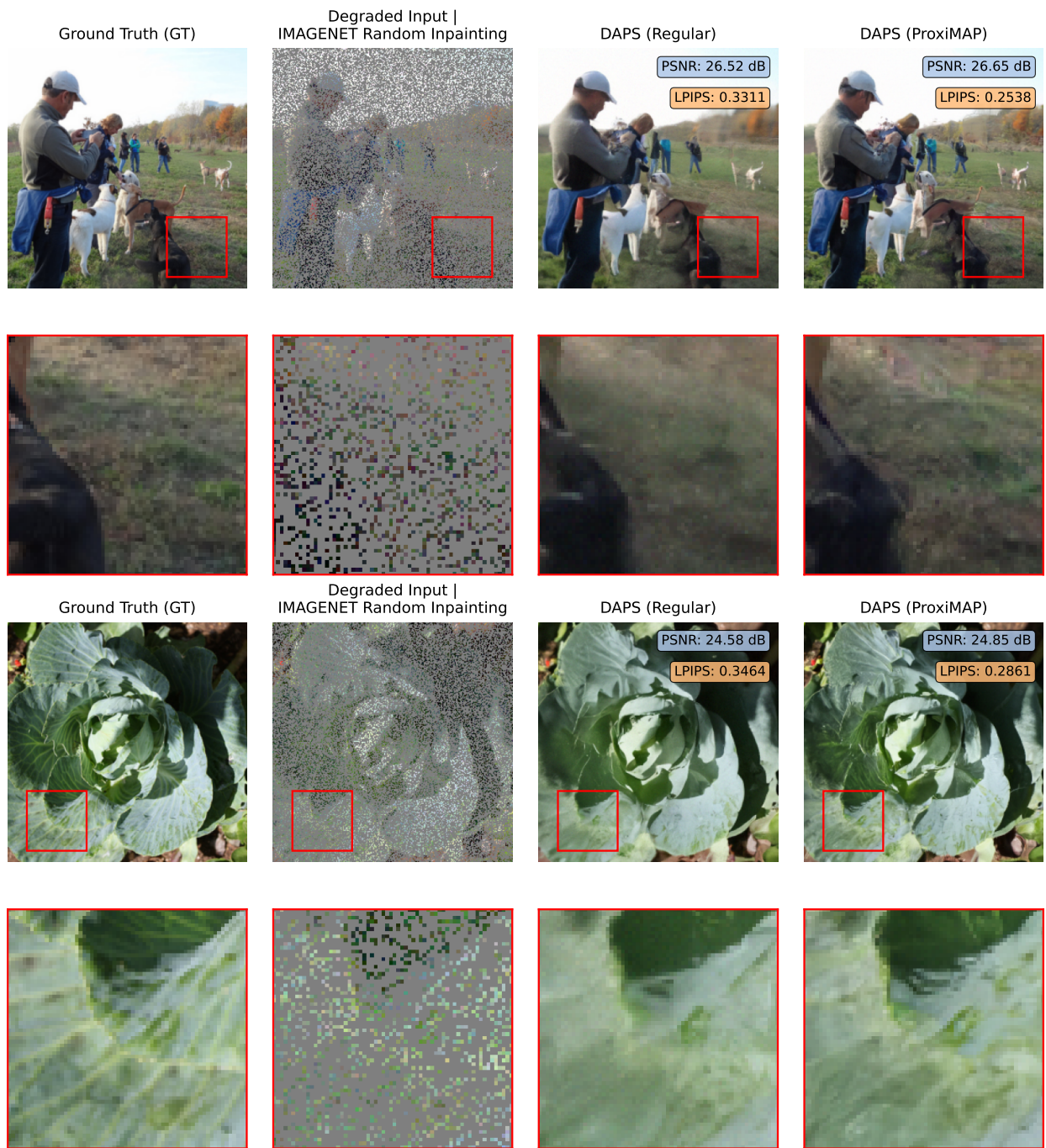


Figure 12: Qualitative results of DAPS on random inpainting. The ProxiMAP variant has a better texture on the image compared to the smoothed MMSE result

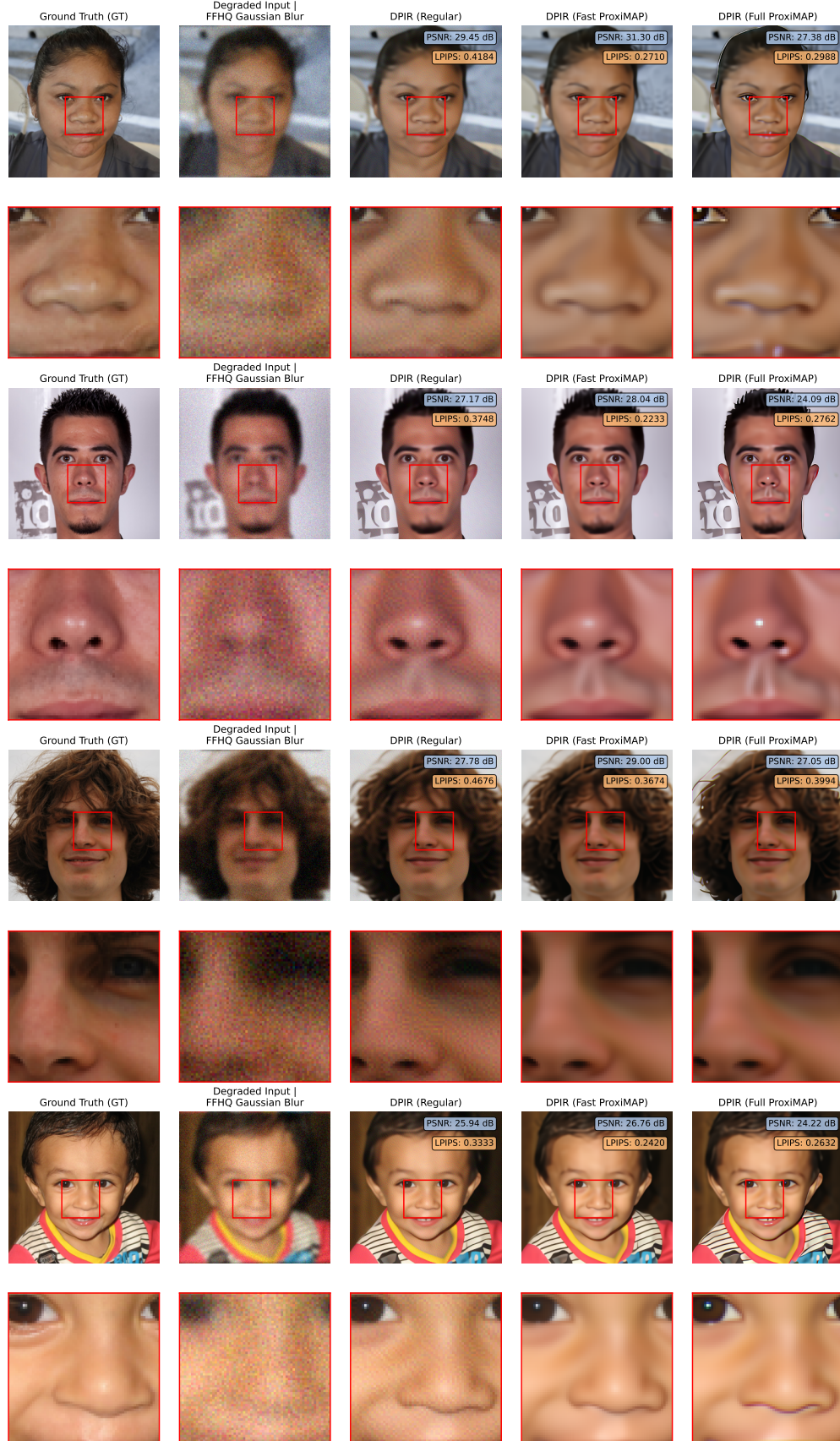


Figure 13: Example of gaussian deblur using DPIR on FFHQ. Some leftover residual noise is removed by using ProxiMAP.

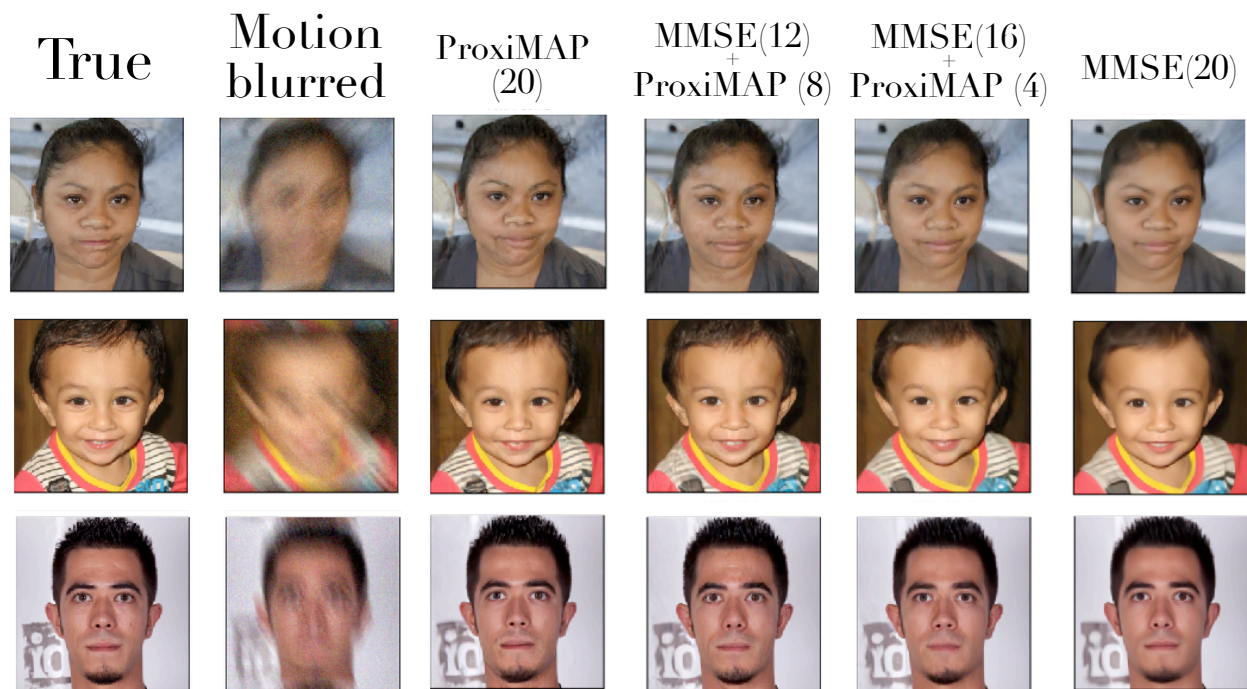


Figure 14: Qualitative visualization for different switch times on motion blur. Panel titles indicate the number of inner iterations performed at each stage with the corresponding algorithm (ProxiMAP or MMSE). Images are sharper for the ProxiMAP variants than the regular MMSE one.

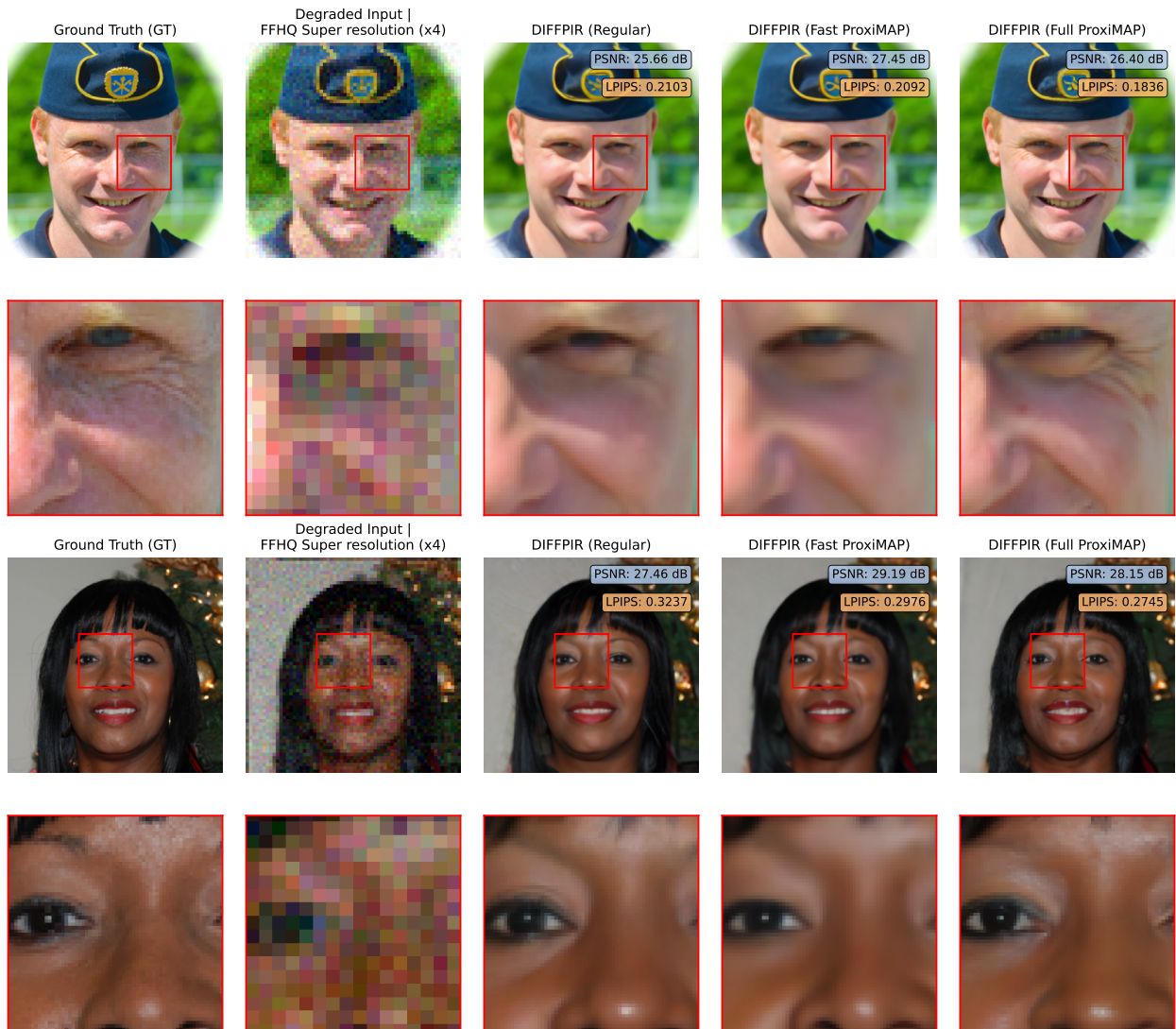


Figure 15: Super resolution using DiffPIR. Here the full ProxiMAP variant seems to work better than the others (as predicted by Fig. 11)

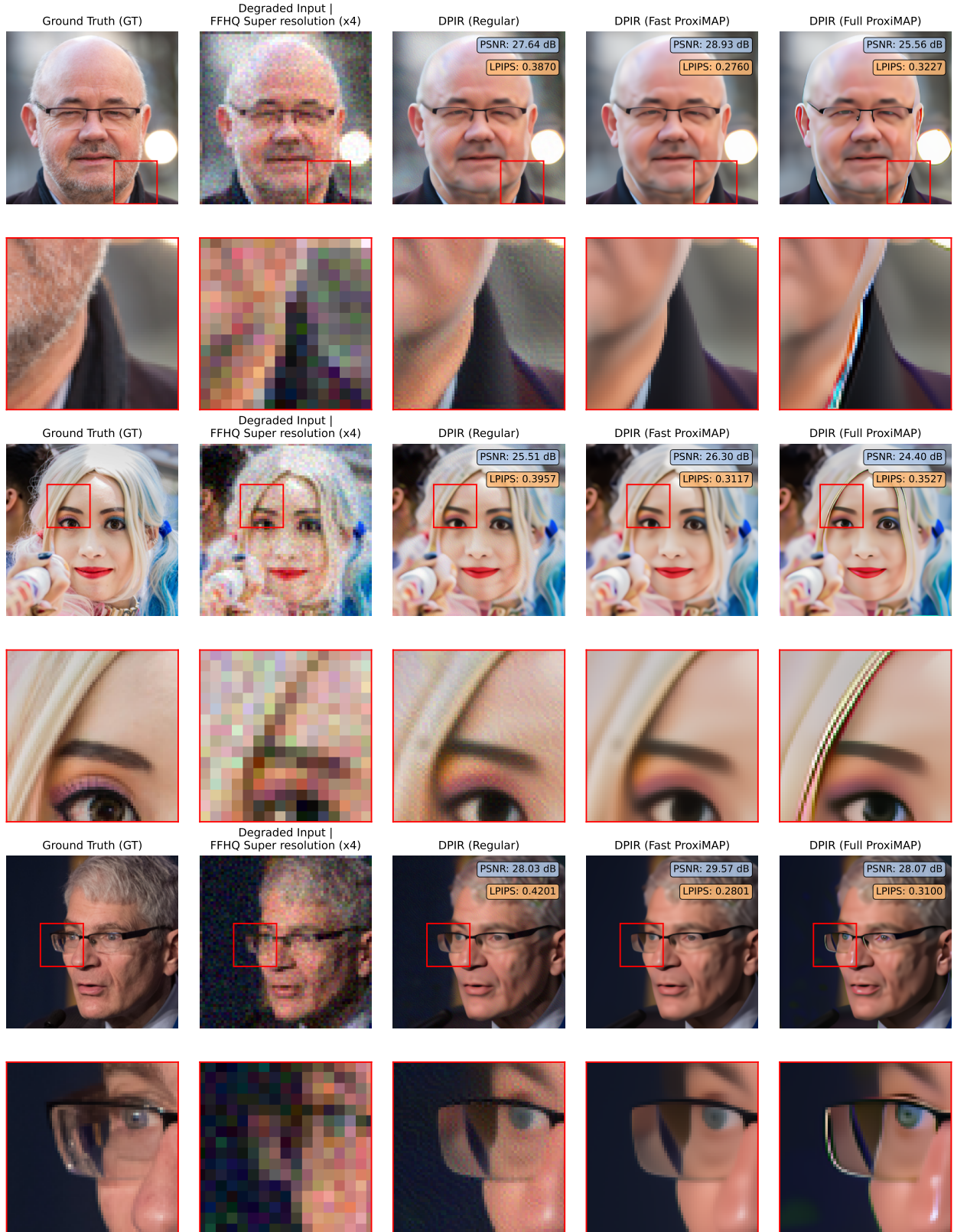


Figure 16: Failure cases for ProxiMAP in DPIR on the super-resolution task. High-frequency artifacts appear along the edges (right column), but are removed when we use the Fast ProxiMAP variant.